Testing and modelling of annealed float glass under quasi-static and dynamic loading

K. Osnes[a,b,*], T. Børvik[a,b], O.S. Hopperstad[a,b]

[a]*Structural Impact Laboratory (SIMLab), Department of Structural Engineering, NTNU, Norwegian University of Science and Technology, NO-7491 Trondheim, Norway*
[b]*Centre for Advanced Structural Analysis (CASA), NTNU, Norwegian University of Science and Technology, NO-7491 Trondheim, Norway*

Abstract

In recent years, a considerable number of studies has been carried out to analyse the behaviour of laminated glass plates under blast loading by the use of the finite element method. This has proven to be quite challenging, as the response of the laminated glass is complex. The fracture strength of the glass layers govern much of the total response; however, a limited effort is often made to selecting this value in the analyses. The current work aims to identify the probabilistic fracture strength of the glass alone as a function of its geometry, boundary conditions and loading situation by the use of a newly proposed strength prediction model. It should be noted that the current study focuses on the initiation of fracture in glass plates, and no effort has been put into the description of crack propagation. To facilitate the validation of the model, three different experimental test series were carried out on annealed float glass. This included quasi-static four point bending tests on relatively small glass specimens, and quasi-static and blast pressure tests on larger glass plates. The experimental work demonstrated that the fracture strength of glass exhibits a large scatter within the same test setup. It also revealed that the fracture strength and its scatter were dependent on the geometry, and the boundary and loading conditions. The strength prediction model was able to successfully capture many of the trends observed in the quasi-static tests. Regarding the blast tests, the model was able to reproduce the experimental results reasonably well.

Keywords: Glass, Brittle fracture, Probabilistics, Numerical simulation, Blast loading

1. Introduction

Annealed float glass is widely used in window systems, but is a brittle material that offers little resistance to the intense blast waves produced by explosions. If the window fails, it breaks into

*Corresponding author
Email address: karoline.osnes@ntnu.no (K. Osnes)

Nomenclature

α	In-plane flaw orientation
δ	Centre displacement in beam
η	Distribution parameter
λ_s	Surface flaw correction factor
μ	Mean of the normal distribution
ν	Poisson's ratio
ϕ	Angle of point on flaw
ρ	Density
ρ_{flaw}	Flaw density
σ	Remote normal tensile stress
σ_n	In-plane normal stresses
σ_x	Normal stresses in x direction
σ_y	Normal stresses in y direction
$\sigma_{f_{max}}$	Maximum tensile stress at failure
$\sigma_{f_{mean}}$	Mean tensile stress at failure
$\sigma_{f_{min}}$	Minimum tensile stress at failure
σ_f	Tensile stress at failure
τ	Incubation time
τ_{xy}	In-plane shear stress
a	Flaw depth
a/c	Flaw shape
a_i	Depth of flaw i
A_{jumbo}	Area of jumbo plate
a_{max}	Maximum flaw depth
b	Decay coefficient
c	Flaw half-length
D_{max}	Maximum centre displacement
E	Young's modulus
F	Applied load
$f(\phi)$	Angular flaw function
F_f	Failure load
h	Thickness
i_+	Impulse of positive pressure phase
K_{IC}	Fracture toughness
K_I	Stress intensity factor for mode I loading
L	Length
L_l	Length of loading span
L_s	Length of support span
N, c_i, w_i	Normalized histogram parameters
N_0	Number of flaws on glass surface
N_i	Number of flaws with $a \geq a_i$
P_0	Atmospheric pressure
P_{max}	Peak reflected overpressure
$P_{r,\,max}$	Peak reflected pressure
$P_r(t)$	Reflected pressure
P_s	Negative overpressure
Q	Flaw shape parameter
R_1, R_2	Random variable from 0 to 1
s	Standard deviation of normal distribution
t	Time
t_a	Arrival time of reflected pressure
t_c	Time of failure frame in model
t_{d+}	Duration of positive pressure phase
t_{d-}	Duration of negative pressure phase
t_{frac}	Time of fracture initiation
v_{frag}	Maximum fragment velocity
w	Width
Y	Geometric flaw shape factor
DIC	Digital Image Correlation
SSD	Sample standard deviation
SSTF	SimLab Shock Tube Facility

numerous sharp fragments that can potentially cause major damage [1]. Laminated glass has been found to be effective at mitigating these risks and is now frequently used to increase the protection level by retaining the fragments on a polymer interlayer upon fracture. The polymer interlayer also provides additional resistance to the blast loading even after the glass layers have fractured [2–5]. Lately, much effort has been made to model laminated glass subjected to blast loading by the use of the Finite Element Method (FEM) [3–6]. This has proven to be challenging, as the behaviour of laminated glass is quite complex and dependent on many factors. These include the modelling of the supports, the material properties and failure criteria of both the glass and the polymer interlayer, and the delamination process between the glass and the polymer.

The identification of the glass plates' fracture strength is not straight forward, and is therefore frequently modelled as deterministic using a fixed fracture stress or strain [3, 5]. This value is often based on a limited number of experimental tests, or simply adjusted to fit a representative experiment. It is widely known that the fracture strength of glass plates is probabilistic due to the presence of micro-structural surface flaws [7]. Fracture initiation in glass plates normally depends on the combination of the properties of the flaws and the applied normal stress. Consequently, the fracture may not occur at the point of maximum applied stress. Additionally, the glass strength will also be dependent on both the geometry of the plate and the boundary and loading conditions [8].

In most commercial Finite Element (FE) codes, the failure modelling is based on a deterministic approach. In other words, the given fracture strength applies to the entire glass plate. If this approach is to be used in a design process of glass, the fracture strength must be carefully chosen. It would naturally be advantageous to know the likelihood of the fracture strength specified in the FE model. The current study aims to obtain the probabilistic fracture strength of any glass plate as a function of its geometry, confinement and loading. This will hopefully make the identification of the fracture strength in an FE model more attainable. Note that no effort has been made to model the crack propagation in this work, and the modelling applies only to the initial fracture strength.

Traditionally, the probabilistic strength of brittle materials is described by the Weibull distribution [9], which requires calibration from experimental data. However, Nurhuda et al. [10] found that experimental tests involving glass plates with different test setups lead to different Weibull parameters. This suggests that the Weibull parameters are not material constants, but are dependent on both the dimension and the loading conditions of the glass specimens. Nevertheless, effort has been made to re-scale these parameters to fit different experiments than the ones from which the parameters were extracted, as in the work by Przybilla et al. [11]. The method proved suitable to convert the fracture stress distribution from a four-point to a three-point bending test series. The potential shortcoming is, however, the need for experimental tests with a sufficiently large population. Otherwise, an accurate description of the statistical distribution is not possible.

Recently, a strength prediction model of annealed glass plates was proposed by Yankelevsky [12], which aims to predict the glass strength without the need of material tests. The model is based on the existence of microscopic surface flaws in glass, and uses Monte Carlo simulations to determine the fracture strength for glass plates under certain loading conditions. It can also predict the origin of failure, and captures that this does not necessarily occur at the point of maximum applied stress. The resulting fracture strength provided by the model showed good correspondence with experimental four-point bending tests. In a further development of the model [13], both fracture strength and origin of fracture proved to be well predicted, when compared to a larger series of four-point bending tests.

The current work proposes a further development of this approach, and includes additional features and adjustments to the original model. In addition, experimental tests on annealed float glass have been carried out to facilitate validation of the strength prediction model. This includes quasi-static four-point bending tests on relatively small glass specimens, and quasi-static and dynamic lateral pressure tests on larger glass plates. The dynamic pressure tests involve subjecting the glass plates to a blast pressure in the SIMLab Shock Tube Facility (SSTF) [14], while the quasi-static pressure tests employ a slowly increasing water pressure. The experimental work shows that the fracture strength of glass depends on both size and loading condition, and has a great variation within the same test setup.

2. Experimental study

2.1. Material

2.1.1. Glass

The glass plates and specimens used in the experimental work are made out of clear soda-lime-silica glass, which has gone through an annealing process. The mechanical properties of glass are dominated by brittle behaviour and glass behaves elastically to the point of failure. Due to the lack of plastic flow in glass, the energy absorption during crack propagation is small compared to e.g. metals [15]. Consequently, fracture in glass typically propagates fast with little chance of crack arrest. The theoretical strength of glass is much larger than its true strength, to which microscopic surface flaws are responsible. The existence of these microscopic flaws causes the material to fail normally in tension, and is also the reason for glass' stochastic fracture strength [8]. Table 1 presents some commonly employed material parameters for soda-lime-silica glass, which are used as nominal values in this work. The fracture toughness K_{IC} relates to the critical stress intensity factor for mode I loading. The stated value is reported in [16], and is based on the work by Wiederhorn [15].

Table 1: Material parameters for soda-lime-silica glass.

Density ρ (kg/m^3)	Young's modulus E (MPa)	Poisson's ratio ν	Fracture toughness K_{IC} ($MPa\sqrt{m}$)
2500 [17]	70000 [17]	0.2 [17]	0.75 [16]

2.1.2. Rubber

In the shock tube tests presented later in this study, Neoprene rubber strips with an International Rubber Hardness Degree (IRHD) of 50±10 were placed on each side of the glass. Both the hardness and dimensions of the rubber strips were chosen based on test methods described in the European Standard for testing of security glazing subjected to blast pressure [18]. In order to recreate the shock tube tests by means of FEM (see Section 4.2), the boundary conditions had to be modelled with sufficient accuracy. Therefore, a series of compression tests was performed on the rubber to retrieve material data. Cylindrical specimens with 6 mm diameter and 4 mm height were tested at three different machine speeds. The tests were carried out in an Instron 5944 testing machine with a 2 kN load cell. Two cameras with a recording rate of 5 Hz were used to obtain the longitudinal and transverse deformation by the use of an in-house tracking algorithm in MATLAB.

The results for a selection of compression tests are presented in Figure 1, which shows the true stress versus logarithmic strain for the three different loading rates. An incompressible material was assumed. Although the rates achieved in the shock tube tests could be higher than the ones presented here, a rate-insensitive and linear-elastic behaviour was later assumed for sufficiently small strains. A linear curve fit yields an initial stiffness of ~ 2 MPa.

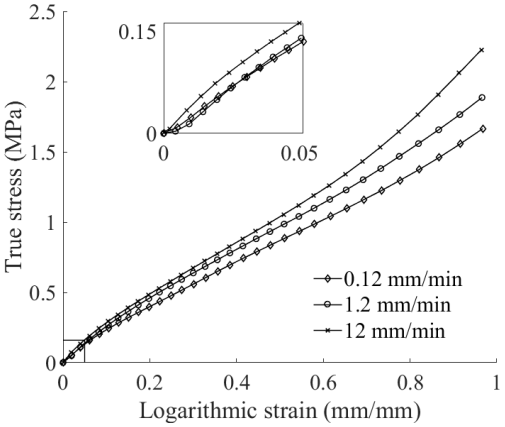

Figure 1: True stress versus logarithmic strain curves for Neoprene rubber at three different machine rates.

2.2. *Quasi-static four-point bending tests*

Since fracture in annealed float glass is a stochastic process, quasi-static four-point bending tests were employed in order to investigate the scatter in material strength. Specimens of three different sizes were tested, and the nominal dimensions can be found in Table 2. The largest deviations from the values stated are 0.4 %, 1.0 % and -1.8 % for the length, width and thickness, respectively. A nominal strain rate of 7×10^{-5} s^{-1} was achieved during testing for all specimen sizes. The specimens were cut with a glass cutter by the manufacturer, and the edges were not treated. In all of the tests, the most damaged edges, i.e., the scoring edges, were placed upwards in order to minimize failure at the edges.

Table 2: Nominal dimensions of specimens undergoing four-point bending.

Specimen	Length L (mm)	Support span L_s (mm)	Loading span L_l (mm)	Width w (mm)	Thickness h (mm)
Large	300	280	140	60	4
Medium	200	180	90	40	4
Small	100	80	40	20	4

Figure 2 shows a schematic of the four-point bending tests. The setup is based on the ASTM standard C1161-13 [19], which is originally intended for testing of advanced ceramics. An Instron 5985 testing machine with a 5 kN load cell was used to load the specimens to failure, while an optoNCDT 2310-50 laser was used to measure the centre point displacement of the glass. Both the support and the loading cylinders were held in place by rubber bands. The cylinders were made out of high strength steel.

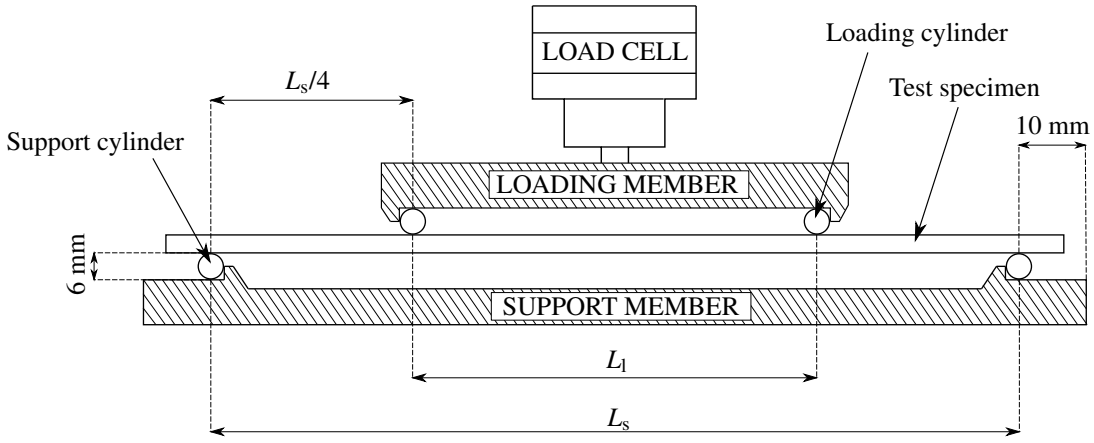

Figure 2: Setup of the four-point bending tests.

After failure of the specimens, the glass fragments were assembled in order to locate where failure initiated. The results for the specimens where failure started at the edges were excluded, as edge effects were not considered in this study. For studies concerning the edge flaws of glass specimens, we refer to the work of e.g. Lindqvist [20]. Figure 3 shows two assembled specimens of medium size after failure; the specimen in Figure 3a failed at the edge and the specimen in Figure 3b, at the face. All edge-failed specimens were identified by crack branching from a point located at the edge, as seen in Figure 3a. A total of 31 specimens of each size were tested, and 20, 21 and 30 tests were recognized as valid for the small, medium and large specimens, respectively. It was observed that the edge-failed specimens had a lower strength than the rest, with a reduction in mean failure load of 46.2 %, 33.1 % and 42.3 % for the small, medium and large specimens, respectively.

(a) (b)

Figure 3: Typical glass specimens after failure in four-point bending tests: (a) failure at the edge, (b) failure at the face.

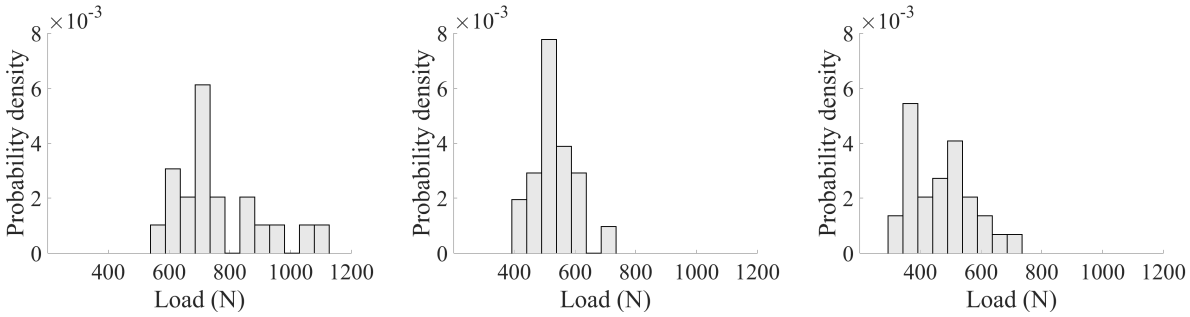

(a) (b) (c)

Figure 4: The probability density distribution of the applied load at failure for a) small b) medium and c) large specimens.

Figure 4 shows histograms of the applied force at failure for the valid bending tests. The ordinate value refers to the probability density, i.e., a normalized occurrence calculated by $c_i/(Nw_i)$, where c_i is the number of elements in the bin, N is the total number of elements and w_i is the width of the bin. For a more attainable comparison of the fracture strength of the three specimen sizes,

the maximum tensile stresses at failure, σ_{f}, were calculated from beam theory as

$$\sigma_f = \frac{3F_{\mathrm{f}}L_{\mathrm{s}}}{4wh^2} \tag{1}$$

where F_{f} is the failure load, L_{s} is the support span, w is the width and h is the thickness of the specimen. This results in multiplying the resulting failure load with the factor 0.22 mm^{-2}, 0.21 mm^{-2} and 0.19 mm^{-2} for the large, medium and small specimens, respectively. The extreme and mean values for the tensile stresses are presented in Table 3.

Table 3: Calculated tensile stresses from beam theory for small, medium and large specimens in the four-point bending tests (MPa).

	Small	Medium	Large
$\sigma_{\mathrm{f_{min}}}$	110.8	86.39	67.70
$\sigma_{\mathrm{f_{mean}}}$	145.2	111.2	103.4
$\sigma_{\mathrm{f_{max}}}$	207.2	144.7	153.8

Naturally, as the number of tests is rather limited, few definite conclusions can be made about the glass strength from the performed bending tests. However, one trend seems to apply, i.e., an increase in material strength with a decrease in surface area.

The bending tests also provided information about the stiffness of the tested glass material. Again from beam theory, Young's modulus E can be calculated as

$$E = \frac{11FL_{\mathrm{s}}^3}{64\delta wh^3} \tag{2}$$

where δ is the centre point displacement related to the applied load F. A mean value of 69.4 GPa was found, which is close to the nominal value stated in Table 1.

2.3. Blast loading

An illustration of an idealized reflected pressure-time history for a structure subjected to a blast wave is shown in Figure 5. The pressure rises abruptly from atmospheric pressure P_0 to the peak reflected pressure $P_{\mathrm{r,\,max}}$ at the arrival time t_{a} over a rise time close to zero. The pressure then decays to the atmospheric pressure P_0 over a duration $t_{\mathrm{d+}}$, and further to a negative overpressure P_{s} and back again to P_0 over a duration $t_{\mathrm{d-}}$. The first pressure phase is referred to as the positive phase, and the last as the negative phase. In the blast tests presented in this study, neither of the glass plates failed during the negative phase. Therefore, the time-window of interest is here limited to the positive phase of the reflected pressure. The positive phase is typically described by the modified Friedlander equation stated as [21]

$$P_{\mathrm{r}}(t) = P_0 + P_{\mathrm{r,\,max}}\left(1 - \frac{t - t_{\mathrm{a}}}{t_{\mathrm{d+}}}\right)\exp\left(\frac{-b\,(t - t_{\mathrm{a}})}{t_{\mathrm{d+}}}\right), \quad t_{\mathrm{a}} < t < t_{\mathrm{a}} + t_{\mathrm{d+}} \tag{3}$$

where b is the decay coefficient responsible for the curvature from maximum reflected pressure $P_{\mathrm{r,\,max}}$. Typical expressions used to describe the negative phase of the blast wave can be found in Aune et al. [22]. The Friedlander equation will be used to describe the blast loads obtained in this study.

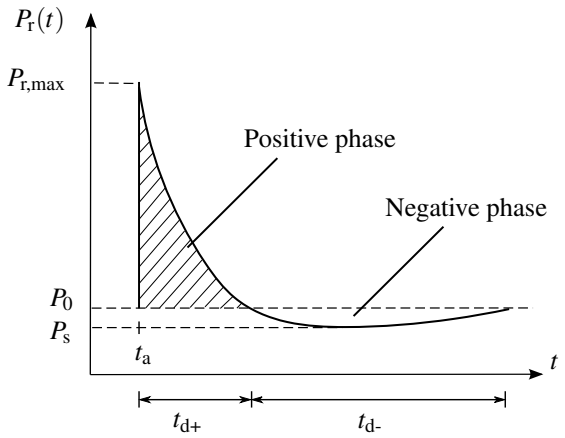

Figure 5: Idealized pressure time history for the reflected blast wave from an explosion [21].

2.4. SIMLab shock tube facility

The SIMLab Shock Tube Facility (SSTF) was used to subject annealed glass plates to blast loading. The SSTF has proven to be a reliable alternative to explosive detonations, and enables a planar pressure loading to plated specimens. A detailed description of the SSTF and its performance can be found in [14]; however, a short description is given herein for completeness.

The purpose of the SSTF is to subject specimens to a pressure history similar to that from a far-field blast event within a controlled laboratory environment. The SSTF consists of a high-pressure chamber (called driver section), and a low-pressure chamber (denoted driven section). The driver and driven sections are separated by one or several diaphragms, which rupture when their capacity is reached. A high air pressure is built up in the driver section, and when the diaphragms fail, a series of pressure waves will run down the driven section and eventually take the form of a characteristic blast wave. When the blast wave reaches the specimen mounted at the rear end, it is reflected, and the reflected overpressure represents the pressure loading of the specimen. The intensity of the pressure load increases with both the build-up pressure and the volume of the driver section. Possible fragments from the specimen after loading and fracture are confined in a dump tank at the end of the driven section. A sketch of the SSTF and the general experimental setup is shown in Figure 6. For the experiments presented in this study, the shortest driver length of 0.27 m was used in order to subject the glass plates to a sufficiently low pressure. The dump tank at the end of the driven section was closed during the experiments, and

two Phantom v1610 high-speed cameras with a recording rate of 24 kHz were placed outside to film through the windows of the tank. To estimate the reflected pressure on the tested glass plates, two piezoelectric pressure sensors were placed 245 mm and 345 mm upstream the plate (see Figure 6a). By assuming constant velocity of the blast wave between the furthest sensor and the plate, the reflected pressure could be determined [14]. The pressure measurements were logged with a frequency of both 500 kHz and 24 kHz. The latter was done in order to synchronize the cameras and the pressure measurements.

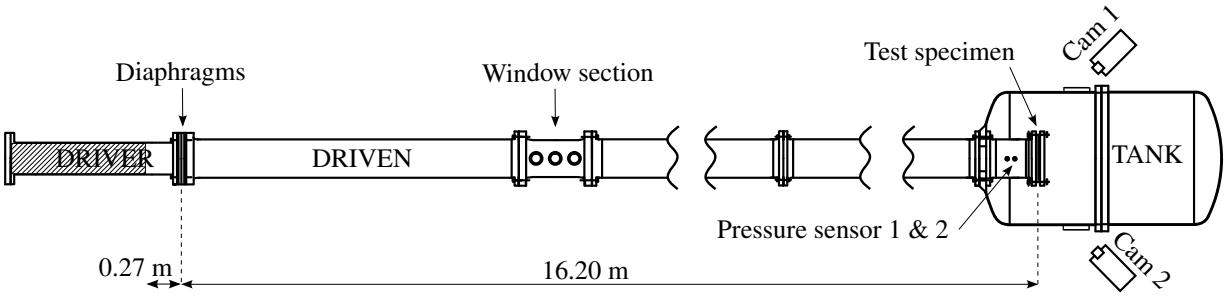

(a)

(b)

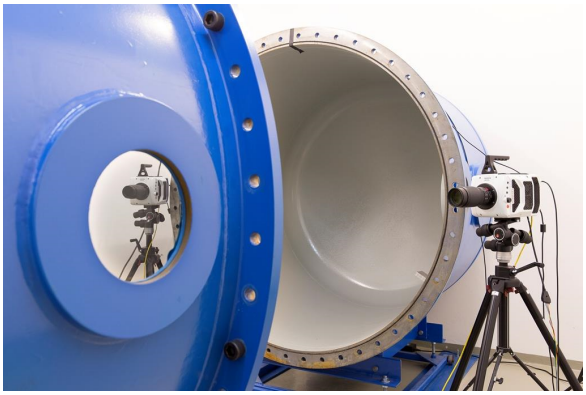

(c)

Figure 6: Test setup in the SIMLab Shock Tube Facility (SSTF) [14]: (a) sketch of the shock tube seen from above, (b) the shock tube seen from the driver, (c) high speed cameras on each side of the tank.

A custom-made fastening system was developed for tests on glass plates in the SSTF, as illustrated in Figure 7. The glass plate is clamped between two 25 mm thick aluminium frames, denoted the inner and outer clamping frame. Neoprene rubber strips with a thickness of 4 mm and a width of 50 mm are glued to the clamping frames and positioned between the glass plate and the aluminium. The tested glass has in-plane dimensions of 400 mm$\times$400 mm, while the loaded area is 300 mm$\times$300 mm. The inner clamping frame is fastened to the end of the shock tube, while the outer frame is fastened with 12 equidistant M24 bolts through $\varnothing$25 mm holes in both frames. For the tests on (3.8 mm thick) float glass, 6.6 mm thick steel washers, or stoppers, are

used between the clamping frames in order to minimize the motion of the outer clamping frame during the tests by properly fasten it, while limiting the clamping pressure on the glass. The steel stoppers are threaded on the bolts, and have an outer diameter of 43 mm. Additionally, a part of the inner clamping frame was milled out to facilitate the setup, and is about 5.7 mm deep.

In the European Standard for testing of security glazing subjected to blast pressure [18], it is stated that a clamping pressure of 14 ± 3 N/cm^2 should be applied. The thickness of the steel stoppers was chosen on the basis of this pressure, as the thickness governed the contraction of the rubber, and further the clamping pressure. To obtain this pressure exactly proved, however, to be challenging due to small variations in the thickness of the glass plates, rubber strips and clamping frames. Nevertheless, the steel stoppers offered proper tightening of the bolts during the tests without damaging the glass plate.

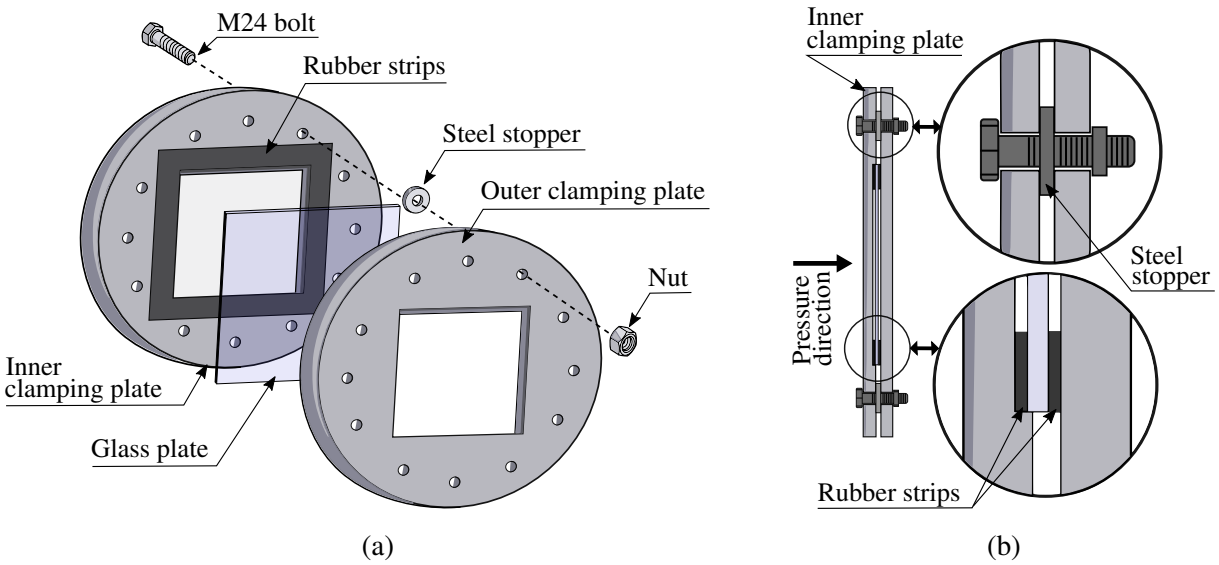

Figure 7: The custom-made fastening system used in the blast experiments on glass in the SSTF: (a) disassembled setup showing one out of 12 bolts, stoppers and nuts, (b) assembled section observed from the side.

2.5. DIC measurements

In the shock tube tests, three-dimensional Digital Image Correlation (3D-DIC) was used to obtain the displacement of the glass plates as well as possible movements of the outer clamping frame. Checkerboard stickers with dimension 12 mm$\times$12 mm were glued to the frame, and white circles with a central black dot, denoted optical targets, were spray-painted on the glass, see Figure 8a. A point-tracking algorithm available in the in-house DIC code eCorr [23] was employed to track the optical targets utilizing photos recorded by the high-speed cameras in the tests. Optimally, a speckle pattern would be painted onto the glass to obtain a complete displacement field

from 3D-DIC instead of point-based displacements. However, this would reduce the visibility of the fracture initiation and propagation in the glass during the tests.

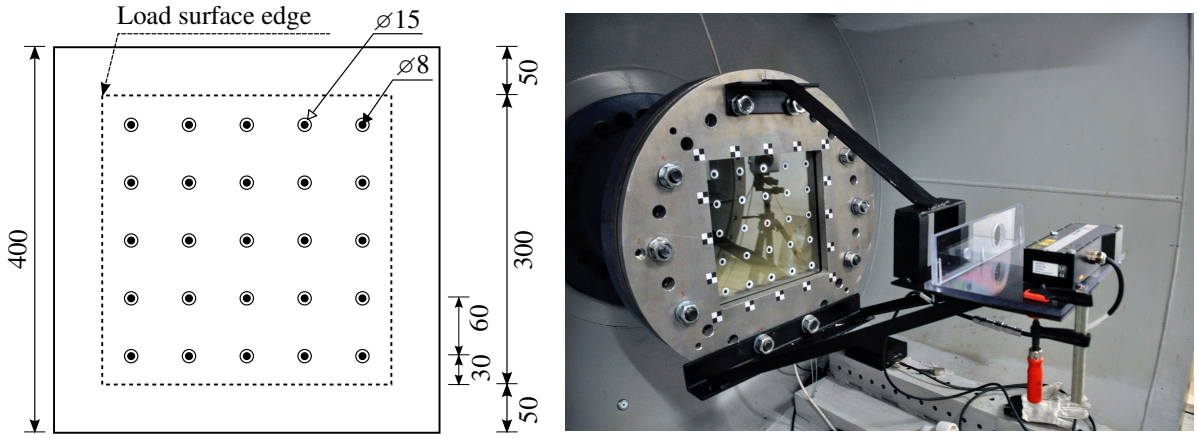

(a) (b)

Figure 8: Test setup for investigation of the point-tracking procedure: (a) optical targets used for point tracking of the glass (dimensions given in mm), (b) laser mounted to the end of the shock tube.

An evaluation of the point-tracking procedure was conducted in a preliminary study. A laser displacement sensor (optoNCDT 2310-50) was fastened to the outer clamping frame, as shown in Figure 8b, and used to measure the displacement in the middle of the glass plate. The same measurement was done by the use of point tracking. Additionally, the movement of the clamping frame was tracked at the checkerboard stickers, also by point tracking. As the laser was mounted to the clamping frame, the middle point displacement obtained by point tracking was corrected for the displacement of the frame. Figure 9 compares the two resulting displacements for a test where the glass did not fracture, and shows that the measurements are in good agreement. Some oscillations are present in the laser data due to vibrations in the laser mount. The results demonstrate that the point-tracking procedure yields reliable displacement data.

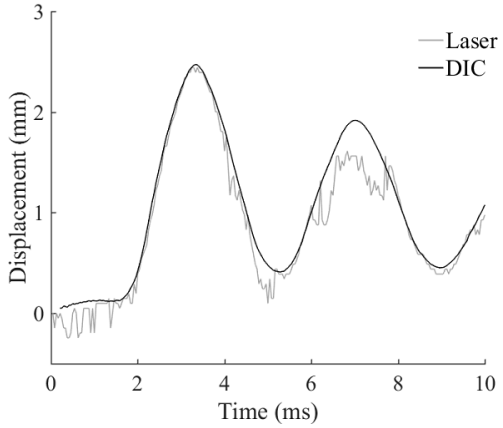

Figure 9: Evaluation of the point-tracking procedure used to measure the mid-point displacement.

2.6. Blast tests

Twelve blast tests were performed in the SSTF on 400 mm×400 mm float glass plates with a thickness of 3.8 mm (mean = 3.805 mm, SSD = 0.01mm). The glass plates and the four-point bending specimens were delivered by the same glass manufacturer. Note that there is a small difference in the mean thickness of the four-point bending specimens and the current glass plates. Table 4 presents maximum reflected overpressure $P_{\max}$, time of fracture initiation t_{frac}, maximum centre displacement before fracture $D_{\max}$, maximum fragment velocity v_{frag}, impulse of the positive phase i_+ and position of fracture initiation. Note that for the failed plates, the positive impulse i_+ was calculated only up until the point of fracture. The tests are divided into three classes (A, B and C), depending on the level of maximum reflected overpressure on the glass. The reflected overpressure was found by employing the logged pressure in the two sensors placed 245 and 345 mm from the plate, denoted sensor 01 and 02, respectively. The Friedlander equation (Equation (3)) was fitted to the pressure data for the non-failed plates, see Figure 10a, and a linear fit up to the time of failure was used for the failed plates, see Figure 10b. Shortly after a glass plate failed in the tests, there was no longer a surface to reflect the pressure wave, and a Friedlander curve fit would not be applicable.

The fragment velocities were calculated based on the measured displacements from the point-tracking procedure. This required that the painted white and black circles were still trackable, which was not always the case. Therefore, these values are somewhat uncertain.

Table 4: Summary of the blast tests on float glass for three classes of loads. Note that $t = 0$ corresponds to the time of arrival t_a of the blast wave.

Test	P_{max} (kPa)	t_{frac} (ms)	D_{max} (mm)	v_{frag} (m/s)	i_+ (kPa·ms)	Fracture initiation
A-01	53.0	1.21	4.52	15.8	59.2	Boundary
A-02	51.6	1.38	5.06	14.7	64.9	Boundary
B-01	63.7	0.88	3.23	24.5	52.5	Face, centre
B-02	64.6	1.25	5.40	18.8	73.2	Boundary
B-03	65.5	1.46	5.64	17.3	86.2	Boundary
B-04	62.5	×	5.44	×	293.9	No fracture
B-05	63.3	1.00	4.29	21.8	58.4	Face, above centre
B-06	62.9	0.92	3.68	19.3	54.1	Boundary
B-07	64.0	1.33	5.77	19.0	76.6	Boundary
B-08	62.9	×	5.96	×	294.2	No fracture
C-01	73.4	1.29	5.89	21.5	86.5	Boundary
C-02	73.2	1.33	6.48	22.3	88.9	Boundary

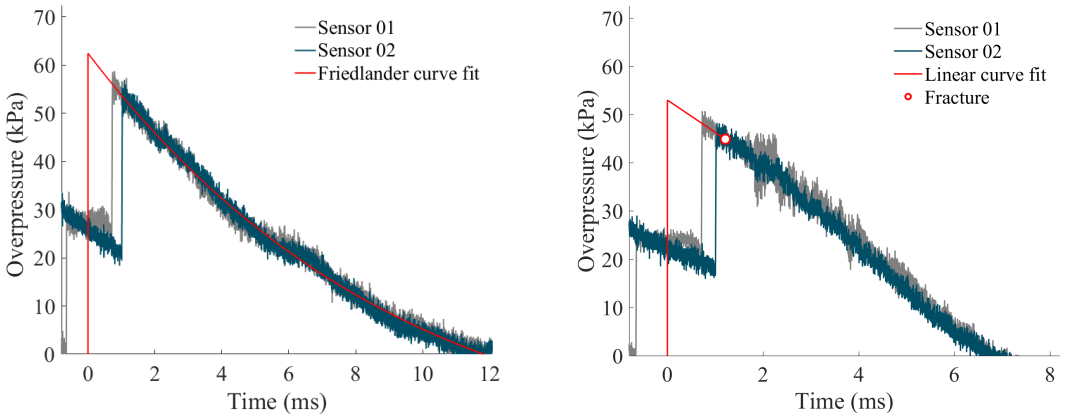

(a) (b)

Figure 10: Pressure measurements in two sensors close to the glass plate, including a representation of the reflected overpressure: (a) Friedlander curve fit for test B-04, (b) linear curve fit for test A-01.

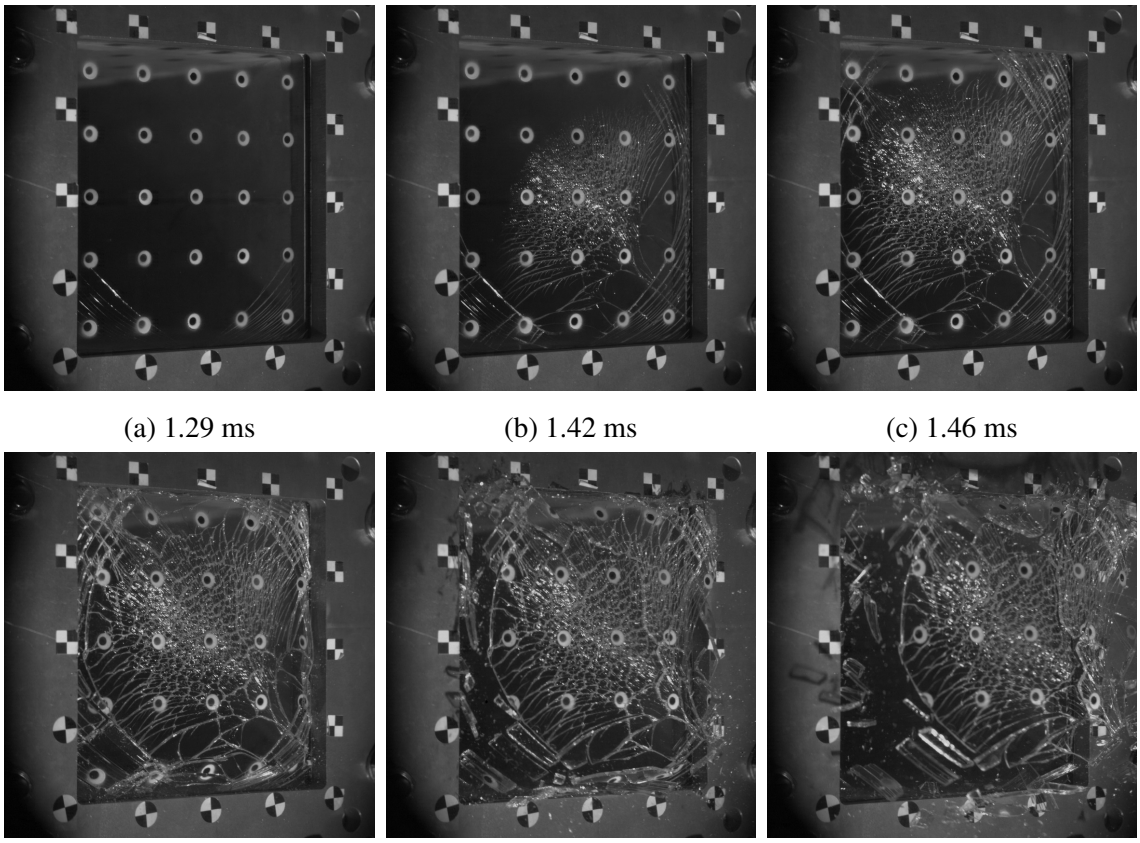

(a) 1.29 ms (b) 1.42 ms (c) 1.46 ms

(d) 4.50 ms (e) 7.58 ms (f) 11.25 ms

Figure 11: Recorded photos in test A-01 captured at various points in time (see subcaptions) after t_a.

In 10 out of 12 tests, the glass plate failed, and for most of the plates, failure initiated at the boundary. More specifically, it initiated under the rubber strips, see Figure 11 for an example. The fracture sequences were similar for all boundary-failed plates, with circumferential crack formations in the corners, and subsequent propagation from the corners to the face. The latter is visualized in Figure 11b-c. For comparison, photos from a test where failure initiated at the face of the plate is shown in Figure 12. In these tests, cracks branched from the point of fracture initiation towards the edges, before circumferential cracks were formed. Note that the accuracy of the specified times is 1/24 ms due to the photo frequency.

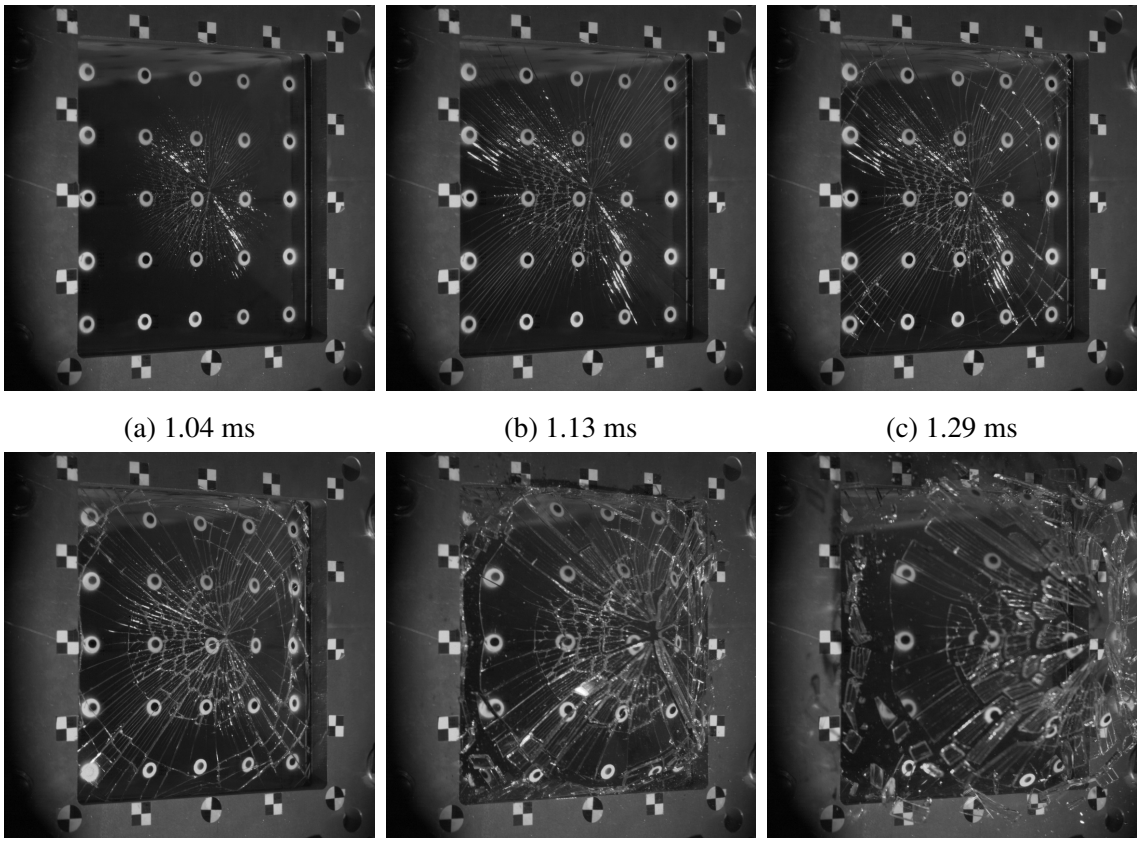

(a) 1.04 ms (b) 1.13 ms (c) 1.29 ms

(d) 2.88 ms (e) 6.17 ms (f) 10 ms

Figure 12: Recorded photos in test B-01 captured at various points in time (see subcaptions) after t_a.

2.7. Quasi-static pressure tests

It was also of interest to investigate the capacity of the glass plates exposed to uniform pressure without the effect of strain rate and inertia. This was done with the use of water pressure, which was slowly built up in a steel chamber with an opening on one side, see Figure 13a. The test setup has many similar features as in the SSTF, including the same type and dimensions of the glass plates, the same loading area, the same dimensions and type of rubber strips, and threading of steel stoppers on bolts fastening the clamping plate. In this case, as for the SSTF, the steel stoppers were used to control the clamping pressure. The thickness of the steel stoppers was here 11.7 mm due to the design of the steel chamber. After tightening of the bolts, the weight of the steel clamping plate (11.1 kg) is transferred to both the stoppers and the bottom rubber strips. The point-tracking procedure was enabled in the tests by using two AVT Prosilica GC2450 cameras and the optical targets on the glass, see Figure 13b. The pressure and camera recordings were synchronized, and logged with a rate of 15 Hz.

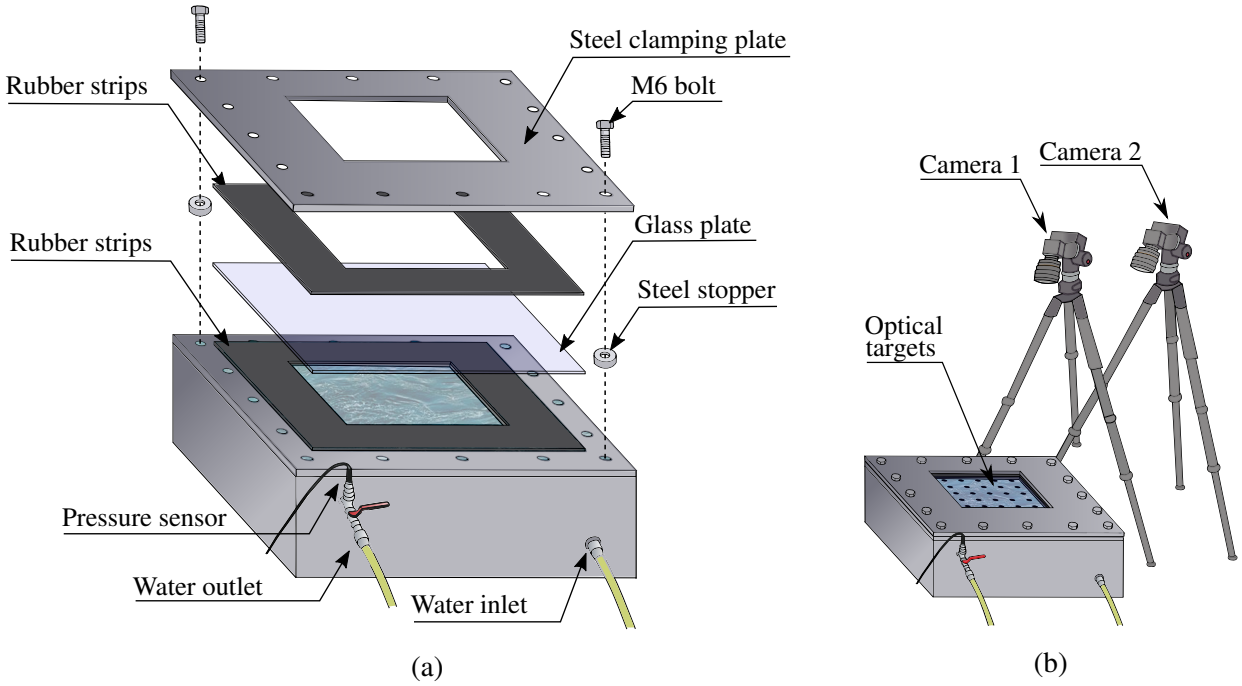

Figure 13: Setup for quasi-static pressure tests: (a) assembly of water pressure chamber, (b) equipment for use of 3D-DIC.

The chamber was filled with water using a hand driven water pump to build up the pressure sufficiently slowly. A total of 11 glass plates were tested, and the resulting pressure-time history for one of these tests (Q-09) is shown in Figure 14a. The oscillations in the pressure are due to the non-continuous filling of water and the fact that the chamber was not completely airtight. A dotted curve plot presenting the pressure-displacement history for the same test is presented in Figure 14b. The displacement corresponds to the upwards movement of the optical target in the middle of the plate. Selected photos from the test are further shown in Figure 15.

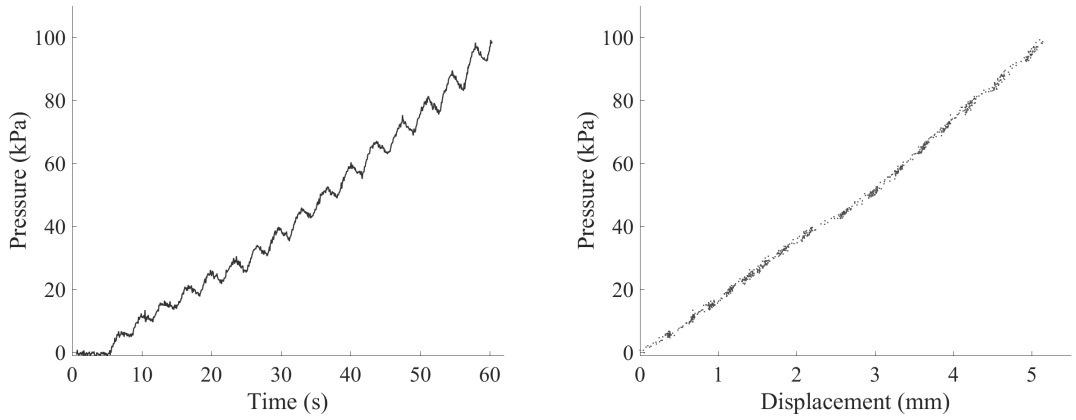

Figure 14: Measurements from quasi-static pressure test Q-09: (a) pressure versus time, (b) pressure versus mid-point displacement.

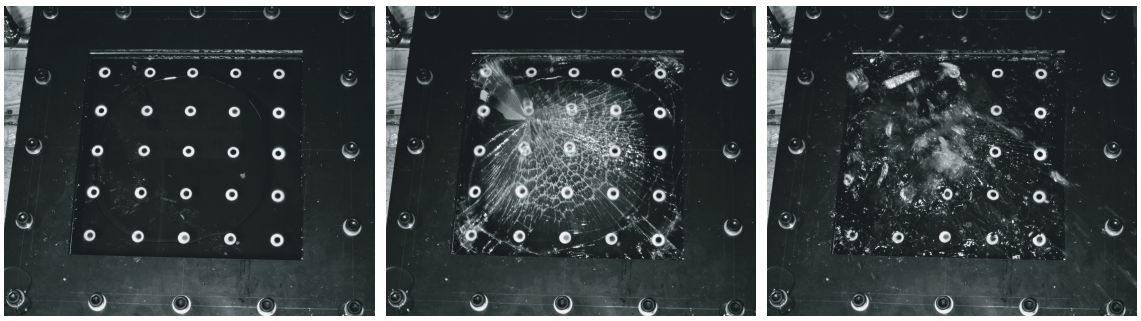

(a) 60.60 s (b) 60.67 s (c) 60.87 s

Figure 15: Recorded photos in quasi-static pressure test Q-09 captured at various points in time (see subcaptions).

The capacity of each glass plate in terms of maximum applied pressure and mid-point displacement, denoted $P_{\max}$ and $D_{\max}$, respectively, is listed in Table 5. Whether failure initiated at the face or boundary is also stated in this table. It is clear that the tested glass plates possessed a large scatter in fracture strength, as the strongest glass plate had more than twice the capacity of the weakest.

Table 5: Summary of results from the quasi-static pressure tests.

Test	P_{max} (kPa)	D_{max} (mm)	Fracture initiation
Q-01	96.9	5.19	Boundary
Q-02	66.5	3.64	Face, above centre
Q-03	65.2	3.54	Boundary
Q-04	48.4	2.69	Face, centre
Q-05	52.5	3.03	Boundary
Q-06	62.4	3.70	Face, below centre
Q-07	61.1	3.53	Face, left for centre
Q-08	83.6	4.62	Boundary
Q-09	98.9	5.19	Face, left and above centre
Q-10	83.8	4.67	Boundary
Q-11	62.3	3.72	Face, above centre

3. Modelling

3.1. Strength prediction model

A stochastic model for predicting the fracture strength of glass plates was recently proposed by Yankelevsky [12]. The strength prediction model presented here is based on this model, where some additional features and adjustments have been included. As for the model by Yankelevsky, stress corrosion and subcritical crack growth [24] are not considered in this study.

3.1.1. Background

Failure in glass is largely driven by the propagation of pre-existing microscopic flaws on the surface. These flaws, also denoted cracks, occur over the entire glass surface and the properties of each individual flaw will vary. The flaw characteristics on a glass surface will also vary from plate to plate. The fracture strength will consequently not be equal for every glass plate, and must therefore be described by a probability function. Moreover, the probability function will depend on the loading conditions and the size of the glass.

When tensile stresses are applied to the glass, and are normal to the flaws, the flaws will open and grow when the stresses are greater than a given threshold. Consequently, glass nearly always fails due to tensile stresses [8]. Because of this, it is natural to adopt the following failure criterion for glass [25]

$$K_{\mathrm{I}} = K_{\mathrm{IC}} \tag{4}$$

where K_{IC} is the fracture toughness for mode I loading, i.e., the opening of a crack. K_{I} is the stress intensity factor for mode I loading, and is used to describe the stress state near the crack tip [26].

It is given by

$$K_{\mathrm{I}} = Y\sigma\sqrt{\pi a} \tag{5}$$

where Y is a geometric factor which depends on the shape of the crack, and σ is the remote tensile stress normal to the crack. For a surface crack, a refers to the depth of the crack, as opposed to an embedded crack where a is the length. For an elliptic surface crack (see Figure 16a) where the crack is small compared to the plate dimensions, Y can be calculated by the empirical expression [27]

$$\begin{aligned} Y &= \frac{\lambda_{\mathrm{s}} f(\phi)}{\sqrt{Q}}, \qquad \lambda_{\mathrm{s}} = \left[1.13 - 0.09\left(\frac{a}{c}\right)\right][1 + 0.1(1-\sin\phi)^2] \\ Q &= 1 + 1.464\left(\frac{a}{c}\right)^{1.65}, \qquad f(\phi) = \left[\sin^2(\phi) + \left(\frac{\mathrm{a}}{\mathrm{c}}\right)^2 \cos^2(\phi)\right]^{\frac{1}{4}} \end{aligned} \tag{6}$$

where c is the half-length of the crack, λ_{s} is the surface correction factor, Q is the flaw shape parameter and $f(\phi)$ is an angular function depending on ϕ. The parameter ϕ defines the angle of a point on the elliptic crack, see Figure 16b.

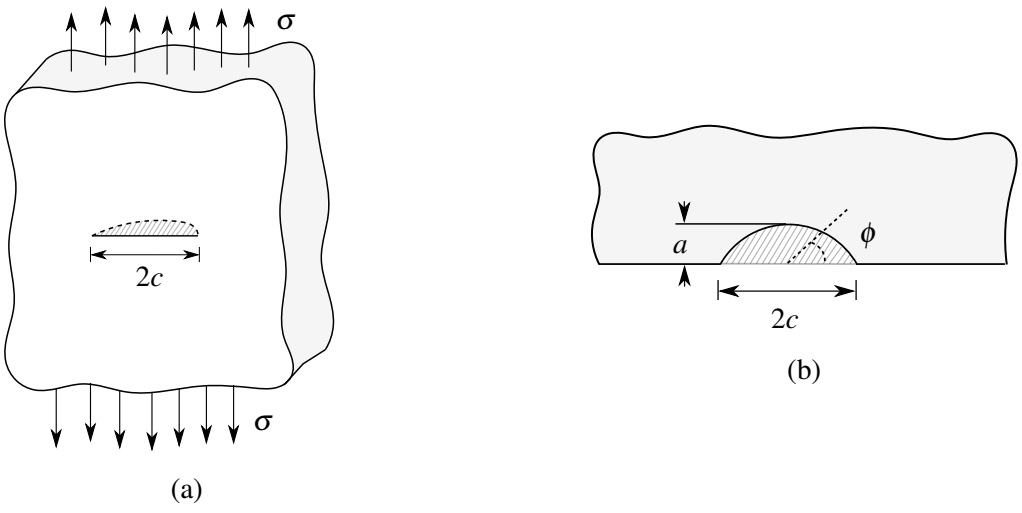

Figure 16: (a) Elliptic surface crack in an infinitely large plate subjected to a remote stress σ. The dashed line refers to the outer edge of the crack placed inside the plate. (b) Section of the plate with denoted crack dimensions. Adapted from [25].

Note that Equation (4) expresses local failure, i.e., the onset of unstable crack growth in one flaw. In the strength prediction model, it is assumed that achieving failure in a single flaw is sufficient to induce failure in the entire glass plate. Since the chance of crack arrest in glass is very small, this is a fair assumption.

For a given loading scenario and geometry of a glass plate, the stress state before failure can be obtained by a finite element analysis. This, together with a small number of selected parameters,

will be the input of the strength prediction model. Subsequently, the model simulates the flaw map, i.e., the distribution of surface flaws including their size, shape, location and orientation. Then, a Monte Carlo simulation is run, varying the flaw map, to establish the statistical strength probability. In the following, the various parts of the flaw map are discussed.

3.1.2. Flaw shape

In order to calculate the stress intensity factor K_{I} at each flaw on the glass surface, the shape of the flaws is required. In the strength prediction model, all flaws are idealized as elliptic, although in reality many may be irregularly shaped. It is further assumed that all cracks have a length-depth-ratio $a/c = 1$. The latter is supported by the work of Levengood [28], which studied the relationship between the fracture strength, the depth of the mirrored region[1] and the depth of the critical flaw in 80 glass specimens. Based on Levengood's results, we obtained the following averaged relationship: $\sigma_{\mathrm{f}}\sqrt{a} = 0.577\ \mathrm{MPa}\sqrt{\mathrm{m}}$, where σ_{f} is the normal stress at failure. The maximum geometric factor Y calculated from Equations (6) for flaws with $a/c = 1$, is equal to 0.729. The resulting critical stress intensity factor K_{IC} is thus

$$K_{\mathrm{IC}} = Y\,\sigma_{\mathrm{f}}\sqrt{a\pi} = 0.729 \cdot 0.577 \cdot \sqrt{\pi} = 0.746\ \mathrm{MPa}\sqrt{\mathrm{m}}$$

which is identical to the value given in Table 1.

3.1.3. Flaw length and density

Yankelevsky [12] assumed that the maximum flaw length typically lies between 100 and 300 µm for standard soda lime glass, and considered 200 µm to be representative. To justify this assumption, the work by Wereszczak et al. [29] was highlighted. This work includes classification of both the density of the surface flaws and the maximum flaw for two soda lime glasses cut by two different procedures. The results are summarized in Table 6, and indicate that both the density and the maximum flaw length depend on the cutting procedure and whether measurements are done on the tin or the air side[2].

[1] The mirrored region is a smooth semi-circular area which forms during glass breakage normal to the applied stress and around the fracture induced surface flaw.

[2] Window glasses of today typically have a tin side and an air side, because one side faces a tin bath through the floating process.

Table 6: Flaw characteristics identified for glass in the work by Wereszczak et al. [29].

Cutting procedure	Side	Density (flaws/cm^2)	Maximum flaw length (μm)
Scored and bent	Air	2.60	133
	Tin	2.37	162
Water jet	Air	1.18	105
	Tin	1.36	195

The tin side of the glasses exhibited somewhat larger flaws than the air side, however, the number of flaws did not favour any of the sides. Moreover, the density of flaws was noticeably larger for the scored and bent plate. Whether this holds in general is uncertain.

It is assumed in the strength model that the flaws are distributed evenly over the glass surface. By using the maximum flaw and density presented in Table 6, and by assuming a uniform positioning, the distance between the flaws is much larger than the dimension of single flaws. This in turn leads to a flaw map with non-interacting cracks [25].

3.1.4. Flaw size distribution

In the work presented by Levengood [28], it was observed that specimens failing for small stresses were the least occurring. This indicates that glass plates exhibit a larger amount of small flaws than large ones. A possible way to describe this tendency, is to employ the distribution function [12]

$$\frac{N_i}{N_0} = \exp\left(\frac{-a_i}{\eta}\right) \tag{7}$$

where N_0 is the total number of flaws on a glass surface, a_i is the depth of a given flaw, N_i is the number of flaws that have depths larger or equal to a_i, and η is a distribution parameter.

The majority of glass used for windows are cut from so-called jumbo plates with nominal lengths of 4500, 5100 or 6000 mm, and widths equal to 3210 mm [30]. It is assumed that there exists only one flaw of maximum size in each of the surfaces of the jumbo plates. N_0 thus becomes the total number of flaws on a jumbo plate surface, and η is given by the following expression

$$\eta = \frac{a_{\max}}{\ln(N_0)} \tag{8}$$

The fracture stresses recorded by Levengood ranged from 57.71 to 351.67 MPa. By employing the relationship $\sigma_f\sqrt{a} = 0.577\ \text{MPa}\sqrt{\text{m}}$, this corresponds to flaw depths from 2.69 to 99.67 μm. In Figure 17, the flaw depth density defined by Equation (7) is compared to the experimental results from [28]. N_0 is set to 80 and $a_{\max}$ to 99.67 μm in accordance with Levengood's tests. Although the test results are not directly comparable with the flaw depth distribution in the jumbo plates, the resemblance of the two curves indicates that the assumed distribution function is reasonable.

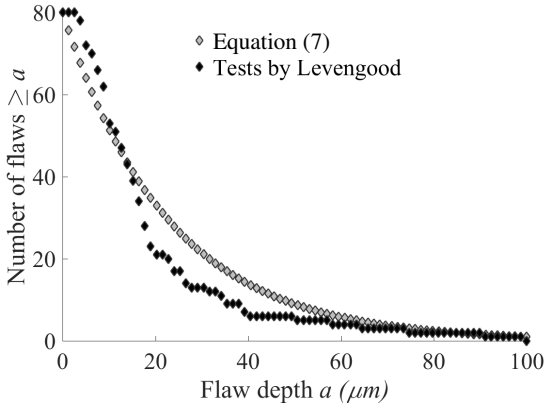

Figure 17: Flaw size distribution governed by Equation (7) versus tests by Levengood [28].

It should be noted that for simple problems, it would be possible to calculate the statistical strength probability directly from the flaw size distribution in Equation 7. However, when the applied stresses in the glass vary in position and time, this is not straightforward. Therefore, we apply a procedure where the statistical strength is instead found by iterative calculations (in a Monte Carlo simulation). Each iteration corresponds to one glass plate.

3.1.5. Flaw orientation

It is fair to assume that the surface flaws do not favour any orientation. Consequently, every individual flaw is given an in-plane orientation pseudo-randomly at an angle α between 0 and π with respect to the x-axis. The remote stresses directed normal to a flaw, denoted σ_n, must therefore be calculated accordingly. σ_n is equal to

$$\sigma_n = \frac{\sigma_x + \sigma_y}{2} + \frac{\sigma_x - \sigma_y}{2}\cos(2\alpha) + \tau_{\mathrm{xy}}\sin(2\alpha) \tag{9}$$

where σ_x and σ_y are the in-plane normal stresses in the x and y direction, respectively, and τ_{xy} is the in-plane shear stress.

3.2. Implementation of the strength prediction model

The following explains the procedure of implementing the strength prediction model, including the preparatory work necessary to apply it. The model itself was implemented in the programming language Python, and the stress state in the glass plates was retrieved by employing the FE software Abaqus [31].

3.2.1. Input

The simulation process starts by defining the dimensions of the glass plate as well as the boundary and loading conditions. An FE analysis is in turn performed (without any failure criterion) to

obtain the stresses in all elements on the glass surface at a sufficient number of evenly spaced time intervals. If shell elements are used, the stresses are taken from the outer integration points, placed at the surface. The failure load and deflection of the glass are usually of interest, and the applied load and relevant displacements must therefore also be obtained by the FE analysis at the specified time intervals. Further, the said output from the FE analysis is used as input in the strength prediction model. Additionally, some parameters must be provided, and the following list summarizes these:

- Fracture toughness K_{IC}
- Flaw shape a/c
- Maximum flaw depth $a_{\max}$
- Flaw density ρ_{flaw}
- Size of the jumbo plate A_{jumbo}
- Number of plates to analyse

The size of the elements used for the glass plate is based on the flaw density and chosen such that each element will contain one flaw. For instance, if the flaw density is chosen as 1/cm^2, the element size will be 10 mm$\times$10 mm. If this element size leads to an overly coarse mesh, the glass plate can be modelled with smaller elements and a clustering technique is used. That is, the same flaw is assigned to a group, or cluster, of neighbouring elements. The clustering procedure is performed in such a way that the chosen flaw density is still preserved. Note that the stresses are still obtained from each element, individually.

3.2.2. Procedure and output

Firstly, a hypothetical jumbo plate of a specified size is assigned N_0 number of flaws with varying depths and orientations on both surfaces. N_0 is equal to the specified flaw density multiplied by the area of the jumbo plate. The flaw depths on each surface of the jumbo plate are calculated based on Equations (7) and (8) as

$$a_i = a_{\max}\left(1 - \frac{\ln(N_i)}{\ln(N_0)}\right), \qquad N_i = R_1(N_0 - 1) + 1, \qquad R_1 \sim U([0,1]) \tag{10}$$

where R_1 refers to a random variable uniformly distributed on [0, 1]. The flaw orientations are further given by

$$\alpha_i = R_2\pi, \qquad R_2 \sim U([0,1]) \tag{11}$$

where R_2 is another random variable uniformly distributed on [0, 1].

Next, each surface element (or cluster of elements) in the glass plate from the FE model is assigned a flaw from the jumbo plate. This would correspond to the plate being cut out from the jumbo plate at a random location. The stresses normal to the flaws in each of the elements are then calculated from Equation (9). The stress intensities K_{I} are further found by Equation (5), where the normal stresses in the elements are treated as remote stresses on the flaws. This is done for every interval until the first element has reached the failure criterion given by Equation (4). The time and stress intensity factor in the failed element corresponding to this interval are denoted t_{c} and $K_{\mathrm{I}}(t_{\mathrm{c}})$, respectively. As $K_{\mathrm{I}}(t_{\mathrm{c}})$ is most likely slightly larger than the fracture toughness K_{IC}, an interpolation of relevant parameters between t_{c} and the previous time $t_{\mathrm{c\text{-}1}}$ is carried out based on the values of the stress intensities, i.e., $K_{\mathrm{I}}(t_{\mathrm{c}})$ and $K_{\mathrm{I}}(t_{\mathrm{c\text{-}1}})$. Next, the glass plate is assigned new flaws, which are taken from the same jumbo plate, and the above procedure is repeated. A visualization of assigned flaw depths and orientations for two glass surfaces from the same jumbo plate are visualized in Figure 18. Here, the surface area is 400 mm$\times$400 mm, and the flaw density is set to 1 flaw/cm^2.

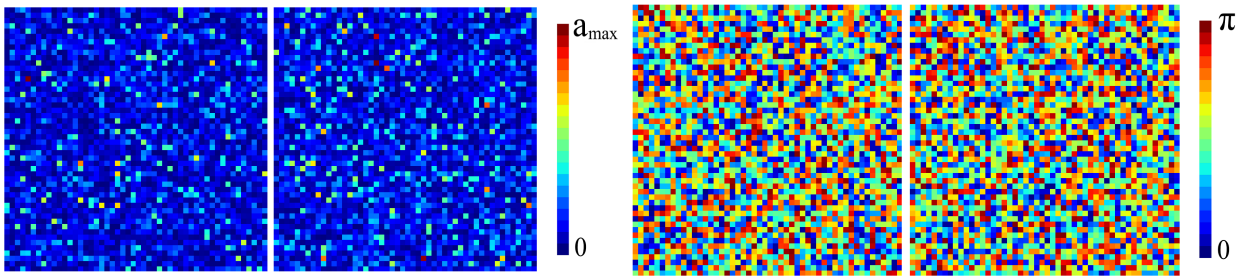

Figure 18: Two randomly selected surfaces with assigned (a) flaw depth and (b) flaw orientation. The corresponding legend is shown on the right hand side of each subfigure.

The above procedure is carried out until all flaws in the jumbo plate have been allocated, and a new one is constructed. The number of different jumbo plates used is dependent on the specified number of plates to analyse. Yankelevsky [12] stated that a total number of at least 5000 plates is required to give a converged and reliable result.

A number of different output parameters are available from the strength prediction model, and the most relevant are listed below. In addition to these, the failure percentage can be found for each studied case. The values of the following parameters are registered for every simulated plate:

- Coordinates of the failed element
- Normal stress at failure

- Displacement at failure
- Applied load at failure
- Time at failure

The above procedure is only valid for static problems, as the failure criterion given by Equation (4) and (5) may not hold for dynamic loading conditions. In the case of glass specimens exposed to rapid loading, the following condition presented in [32] is adopted

$$\frac{1}{\tau}\int_{t-\tau}^{t} K_{\mathrm{I}}(\bar{t})d\bar{t} \geq K_{\mathrm{IC}} \tag{12}$$

Here, τ is denoted the incubation time, or the microstructural fracture time, and is in this case interpreted as the minimum time required to initiate crack growth. Additionally, the criterion is employed to avoid that spurious peaks of stress result in failure of the glass. In order to introduce the aforementioned dynamic fracture criterion in the strength prediction model, it is discretized. Hence, to achieve failure in an element, the averaged value of the stress intensity K_{I} over a period greater than τ must be larger than or equal to the fracture toughness K_{IC}. This criterion naturally requires the determination of the incubation τ. Unfortunately, the authors have not succeeded in finding any records of this parameter for soda-lime glass in the literature. However, as a comparison, a values of 9 µs has been found for Homalite-100 [32].

4. Numerical study

4.1. Quasi-static four-point bending tests

In the following, the strength prediction model is employed in an attempt to find the strength distribution of the four-point bending tests presented in Section 2.2. The bending tests were first recreated in an Abaqus simulation, such that the stress state history could be used as input in the strength prediction model. Shell elements were employed for the glass specimens, while the loading and support cylinders were modelled as analytical rigid surfaces. The dimensions of the glass corresponded to the nominal values given in Table 2, while the element size was set to 1.25 mm, 2.5 mm and 5 mm for the small, medium and large specimens, respectively. Simpson's integration rule was employed with the use of 5 integration points over the thickness. The glass was modelled as linear-elastic with material parameters given in Table 1. The input parameters for the strength prediction model itself are presented in Table 7.

Table 7: Input parameters for the strength prediction model

K_{IC}	a/c	$a_{\max}$	ρ_{flaw}	A_{jumbo}	Number of plates
0.75 MPa$\sqrt{m}$	1	100 µm	2 flaws/cm^2	3210×6000 mm^2	5,000

Figure 19 shows the histograms of the applied load at failure determined by the strength prediction model for the three specimen sizes. For comparison, the forces obtained in the laboratory tests are also included in the figure. Note that the ordinate, denoted probability density, refers to an occurrence, which is normalized to the model and test results individually. As can be seen, the failure loads from the tests are all within the capacity given by the strength prediction model.

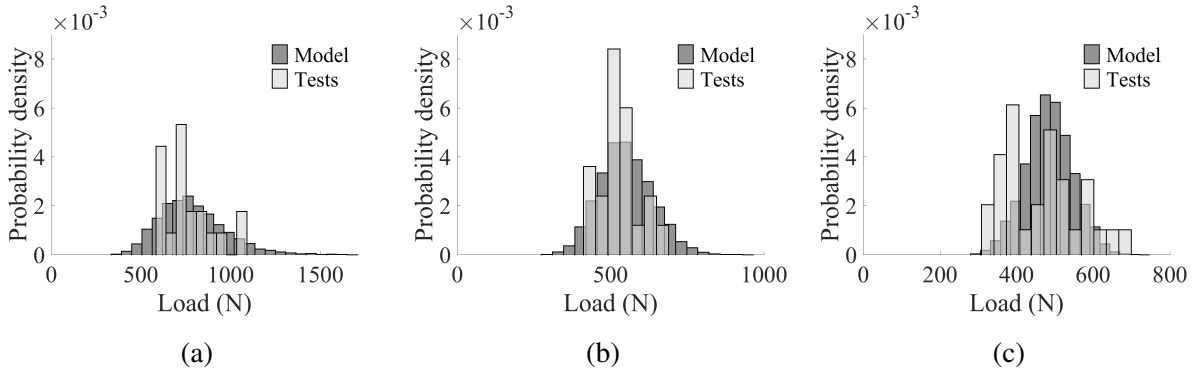

Figure 19: The probability density distribution of forces at failure determined by the strength prediction model and laboratory tests for (a) small, (b) medium and (c) large specimens in four-point bending.

The normal stresses at failure determined by the strength prediction model are presented in Figure 20. To facilitate an easier interpretation and comparison of the results, fitted normal probability density functions are included. The corresponding parameters are presented in the same figure, where μ and s are the mean and standard deviation of the normal distribution. As the normal distribution was found to give a better fit than e.g. the Weibull distribution, this was chosen in this study. However, both distributions highlighted the same trends of the strength prediction model. That is, a decreased surface area results in an increased mean and scatter of the fracture strength.

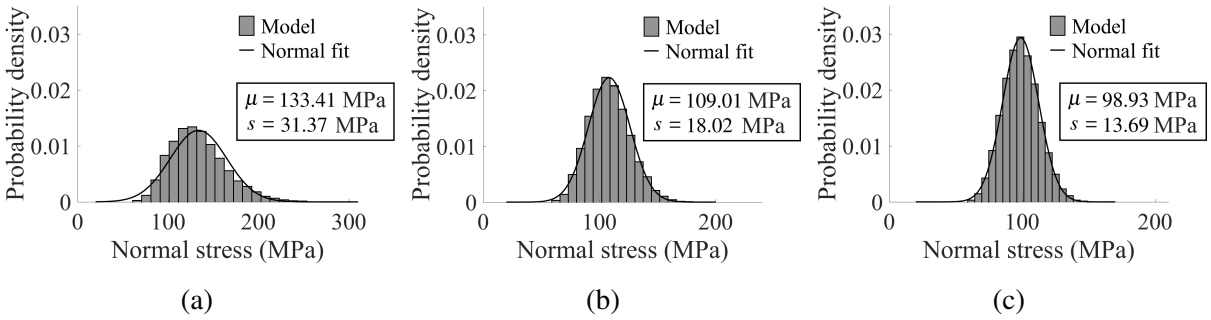

Figure 20: The probability density distribution of normal stresses at failure determined by the strength prediction model for (a) small, (b) medium and (c) large specimens in four-point bending. A normal distribution function has also been fitted to the results.

4.2. Shock tube tests

As for the four-point bending tests, FE simulations of the shock tube experiments were first run in order to obtain the stress state throughout the tests. This was in turn used as input in the strength prediction model. The following subsection describes the FE model of the test setup built in Abaqus.

4.2.1. FE model

The FE model of the test setup was based on several simplifications. Firstly, only the glass plate and rubber strips were modelled, see Figure 21a. The clamping frames and steel stoppers were indirectly included in the model by restricting movement of the outer rubber surfaces in all directions. This is a fair assumption as the rubber strips were glued to the clamping frames and the movement of the clamping frames was close to zero during the tests. Secondly, to account for the clamping pressure in the test set up, the rubber was translated 0.005 mm towards the glass before loading. Thirdly, the rubber was modelled by a linear-elastic material model with a Young's modulus of 2 MPa and a Poisson's ratio of 0.46. Lastly, owing to the assumed linear-elastic behaviour of the rubber, only one (fully integrated) solid element was appropriate in the thickness direction. In order to properly describe the motion of the rubber along the frame, the elements had a cubic shape. The glass was modelled with 5 mm $\times$ 5 mm shell elements, using the Simpson's integration rule with five integration points over the thickness. The material was chosen as linear-elastic with parameters in Table 1. It should be made clear that Young's modulus for glass is relatively insensitive to strain rate, as found by e.g. Zhang et al. [33], which makes it appropriate to use the static value. Note also that only a quarter of the plate could have been modelled due to symmetry. However, this was not done as each element was to be assigned an individual flaw.

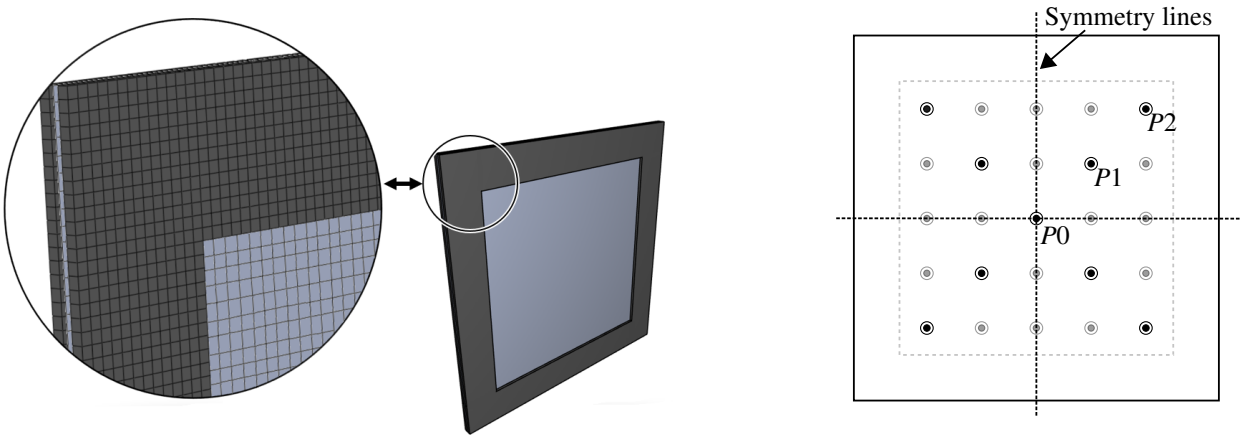

Figure 21: The FE model of the test setup in the SSTF: (a) illustrating the mesh sizes, (b) illustrating points tracked in the FE model and the experiments, including symmetry lines.

Three different loading scenarios were simulated; specifically the pressure histories obtained in test A-01, B-04 and C-01. To ensure that the FE models provided the correct behaviour, displacements in points corresponding to nine optical targets were compared to the DIC measurements. The nine points are shown in Figure 21b, and are limited to three points in the FE model due to ideal symmetry of the deflection. The points are referred to as P0, P1 and P2. The displacements over time in tests A-01, B-04 and C-01 and the corresponding FE simulations are shown in Figure 22.

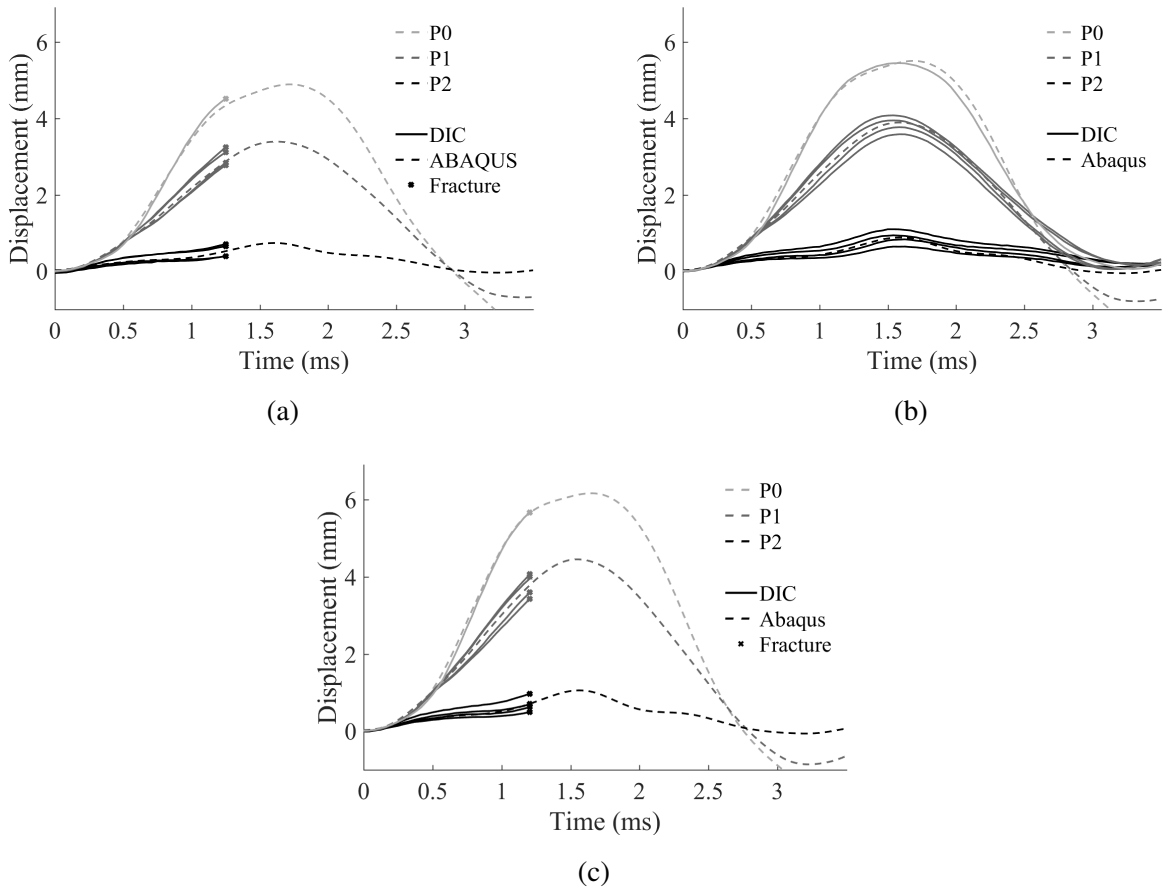

Figure 22: Displacements from DIC and Abaqus simulations in points P0-P2 for tests (a) A-01, (b) B-04, (c) C-01.

The dashed and solid lines refer to the FE model and the experimental tests, respectively. As can be seen, only test B-04 did not fracture at some point, and could therefore be compared throughout the entire course of displacement. The simulation fits well with the experimental test, however, there are some discrepancies after maximum displacement. As fracture will occur in the glass before this point, this is irrelevant in the use of the strength prediction model. Simulations of test A-01 and C-01 also seem to match well before fracture. Consequently, the stress states from these simulations are used as input in the strength prediction model.

4.2.2. Strength prediction

The input parameters of the strength prediction model used for the shock tube tests were the same as for the four-point bending tests, with the exception of one additional parameter, the incubation time τ. This value was merely chosen to be 10 µs. It proved, however, that the strength prediction model was not sensitive for a moderate change in τ.

In the four-point bending and quasi-static pressure tests, the load was gradually increased

such that the ultimate capacity of the tested glass plates could be found. This was not the case for the shock tube tests, and the predicted and measured fracture strength could therefore not be directly compared. Instead, other properties were studied, such as the location and time of fracture initiation, and failure percentage.

Figure 23a illustrates the predicted fracture locations for test A-01. The glass plates experienced tensile stresses on both sides, and the results distinguish therefore between failure on the front and back side of the plate. The back refers, in this study, to the side directly exposed to the pressure load. Figure 23b and 23c illustrate the recurrence of the fracture locations by means of coordinate values in a histogram. The ordinate refers to the number of fictitious glass plates tested. As shown, most plates failed at the front and centre of the plate and the positioning is in addition symmetric. Compared to the actual shock tube tests, the location of front failures agreed well, as it occurred within the area proposed by the strength prediction model. Whether the position of back failure is in agreement with the tests was difficult to determine as the failure initiation occurred under the rubber strips.

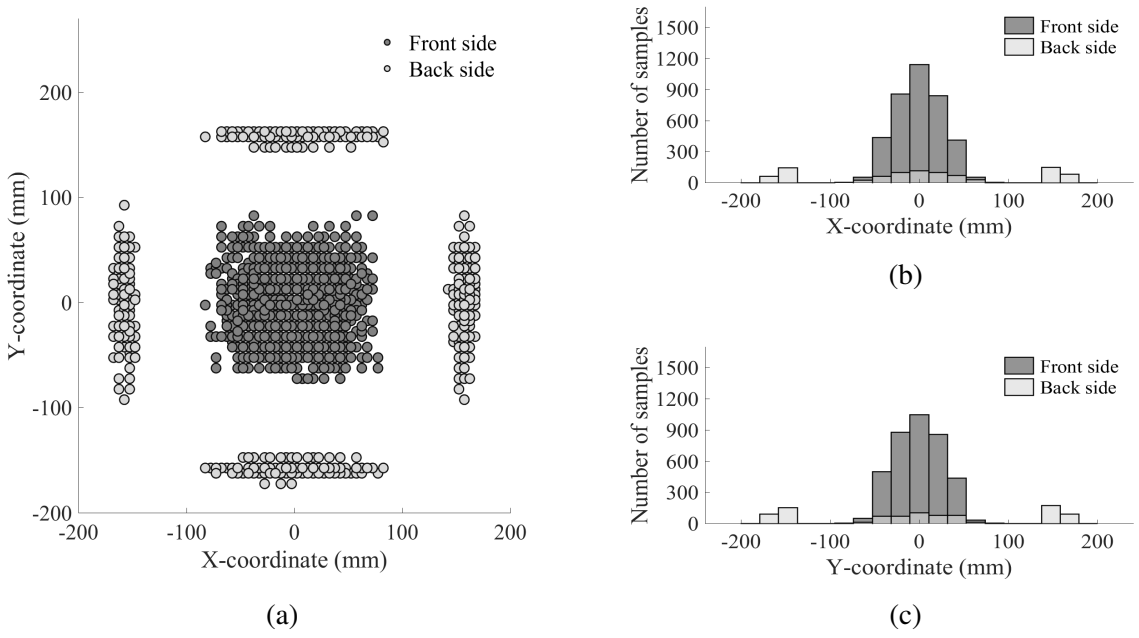

Figure 23: Location of fracture initiation determined by the strength prediction model for test A-01 visualized as: (a) a surface map, (b) a histogram of occurrence on the X-axis, (c) a histogram of occurrence on the Y-axis. The origin is set at the plate's centre.

The failure percentages provided by the strength prediction model for tests A-01, B-04 and C-01 are presented in the first part of Table 8. As a comparison, the failure percentage for the actual tests of class A, B and C were 100 % (2/2), 75 % (6/8) and 100 % (2/2), respectively. The

percentage of plates that failed at the back side is also stated, which in the actual tests proved to be 100 % (2/2), 50 % (4/8) and 100 % (2/2). Thus, the location of failure provided by the strength prediction model was not in particularly good agreement with the test results. However, it should be noted that to draw any definite conclusions, a much larger number of experimental tests must be carried out. Nevertheless, there are various possible reasons for the discrepancy, such as the glass being in direct contact with sharp edges of the clamping plate during the test. However, it may also be due to dynamic effects that are not sufficiently accounted for in the model. The strength of glass is generally increased when exposed to high strain rates [33, 34], and the use of the criterion in Equation (12) may not be suitable to correctly capture this trend. A rather limited study was thus conducted to investigate the effect of an increased fracture toughness, K_{IC}. The input of K_{IC} was set to 0.8 MPa$\sqrt{\mathrm{m}}$, and the resulting failure percentage for test A-01 and B-04 was decreased to 77.7 and 99.2 %, respectively, while the failure percentage for C-01 was unchanged. The failure percentages corresponding to the back of the plates were moderately increased for all tests, specifically 22.2 %, 9.50 % and 4.13 % for A-01, B-04 and C-01, respectively. Note that the fracture toughness should in reality depend on the strain rate rather than being kept constant.

Table 8: Failure percentages and time of fracture initiation t_{frac} determined by the strength prediction model for tests A-01, B-04 and C-01.

	Failure percentage		Time of fracture initiation t_{frac}	
Test	Total (%)	Back side (%)	Front side (ms)	Back side (ms)
A-01	94.2	19.8	0.88-1.92	0.95-1.73
B-04	99.8	4.62	0.82-1.71	0.85-1.54
C-01	100	3.71	0.76-1.41	0.75-1.33

Time of fracture is directly comparable in this case, and the range of predicted times for test A-01, B-04 and C-01 is shown in the last part of Table 8. The results are divided into back and front fracture initiation. For all tests in class A, B and C, the experimental time of fracture lies within or is equal to the predicted extreme values, see Table 4. An increase in fracture toughness, K_{IC}, to 0.8 MPa$\sqrt{\mathrm{m}}$ resulted in a somewhat increased time of fracture. However, the experimental values still remained within the predicted time ranges. The predicted normal stresses at failure for tests A-01, B-04 and C-01 are further shown in Figure 24, and are divided into front and back failures. Here, it is clearly seen that for plates exposed to a lower peak reflected pressure $P_{\mathrm{r,\,max}}$, a larger number of the plates failed at the back side.

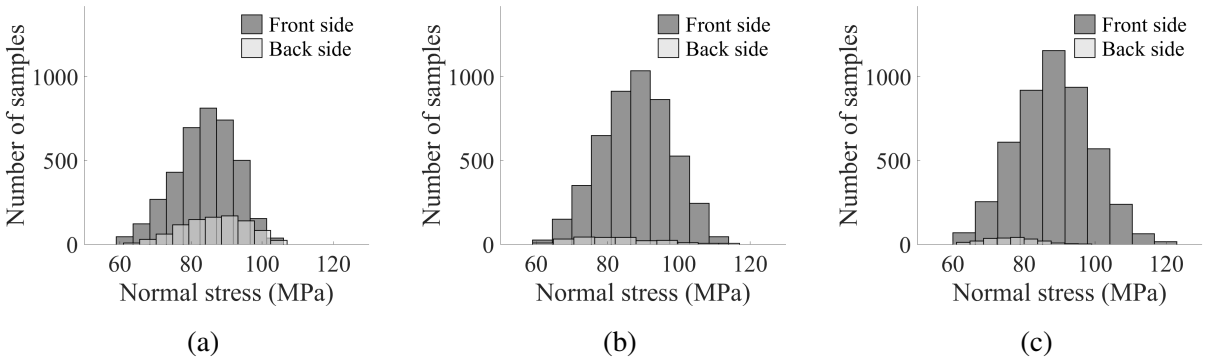

Figure 24: The distribution of normal stresses at failure determined by the strength prediction model for tests (a) A-01, (b) B-04, (c) C-01.

Figure 25 further includes a normal probability density function fitted to the results for test C-01. The parameters of the fitting are also presented in the figure. Compared to the four-point bending tests, both the scatter and fracture stress are decreased, which was expected due to the rather large increase in surface area.

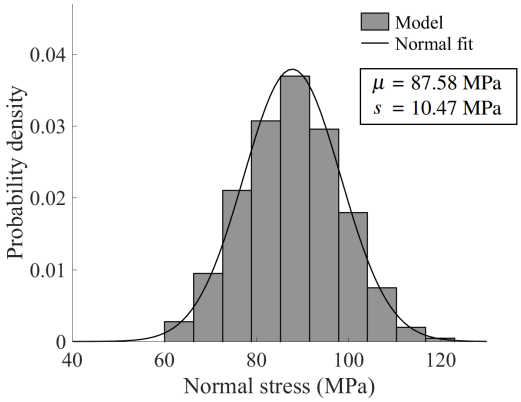

Figure 25: The probability density distribution of normal stresses at failure determined by the strength prediction model for test C-01. A normal distribution function has also been fitted to the results.

4.3. Quasi-static pressure tests

Finally, the strength prediction model is employed to find the strength distribution of the quasi-static pressure tests presented in Section 2.7. As for the previous tests, an Abaqus model of the test setup was first established. The model was the same as for the shock tube tests, except that the load was applied smoothly over a much longer period of time. Additionally, the weight of the clamping plate was applied to the glass edges as a uniform pressure.

To ensure that the Abaqus model provided the correct behaviour, the pressure-displacement histories from the simulation and test Q-09 were compared. The displacements were taken from three points corresponding to P0, P1 and P2 in Figure 21b. Figure 26 presents the resulting curves, where the dotted lines refer to the test, and the solid lines to the Abaqus simulation. As the curves are relatively coincident, we assume that the Abaqus simulation manages to describe the stress state in the plates up to fracture. Consequently, the stress state from the simulation was used as input for the strength prediction model. The input parameters were the same as for the four-point bending tests.

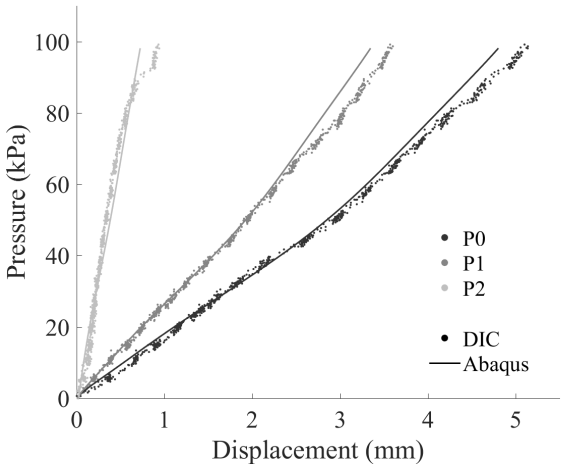

Figure 26: Pressure versus displacement curves from DIC measurements and Abaqus simulations in points P0-P2 for test Q-09.

Figure 27 shows the location of the fracture initiation determined by the strength prediction model. The results are similar to those from the shock tube tests; however, the percentage of failure at the back side is larger for the current tests. Here, 34.3 % failed at the back, while for the C-01 shock tube test, this value was 3.71 %. As for the shock tube tests, the locations of all front failures for the quasi-static pressure tests occurred within the area estimated by the strength prediction model.

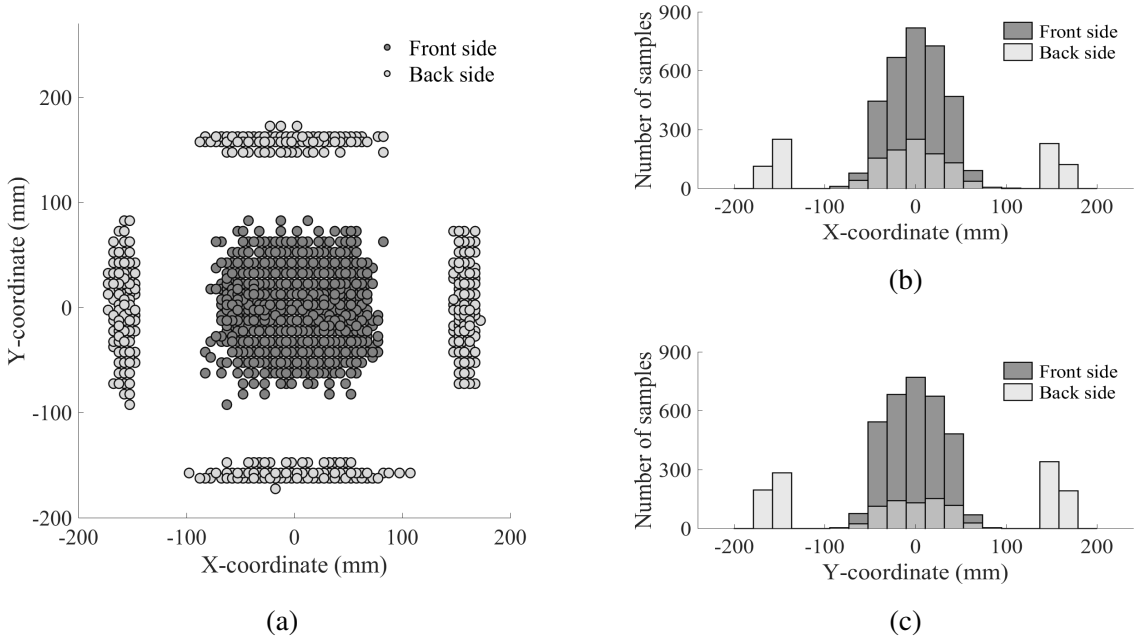

Figure 27: Location of fracture initiation determined by the strength prediction model for the quasi-static pressure tests visualized as: (a) a surface map, (b) a histogram of occurrence on the X-axis, (c) a histogram of occurrence on the Y-axis. The origin is set at the plate's centre.

The applied pressures at failure determined by the strength prediction model, together with the pressures obtained in the tests, are presented in Figure 28 as a histogram. Note that the ordinate, denoted probability density, refers to an occurrence, which is normalized to the model and test results individually. The two tests Q-04 and Q-05 ended up on the outside of the model prediction. A possible reason for this could be that the prescribed initial flaws are smaller than the ones occurring in the tested glass plates. However, it may also imply that there are some effects that are not properly taken into account in the strength prediction model, such as subcritical crack growth. As the quasi-static tests took up to a minute to finish, it is possible that the initial flaws grew stably during the loading, and a smaller flaw size was required to induce failure.

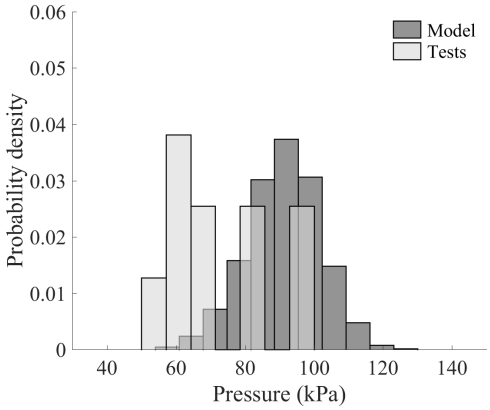

Figure 28: The probability density distribution of applied pressures at failure determined by the strength prediction model and laboratory tests for the quasi-static pressure tests.

A histogram of the resulting normal stresses at failure is presented in Figure 29a, and is divided into occurrences on the front and the back side of the glass plates. Failure at the largest value of normal stresses occurred in this case at the back side of the plate, while the smallest took place at the front. A histogram combining both sides, together with a fitted normal probability density function can be viewed in Figure 29b. The parameters of the fitting are also presented. It should be mentioned that the probability density was almost identical when excluding the weight of the steel clamping plate. Compared to the shock tube tests, both the scatter and the fracture strength are slightly smaller.

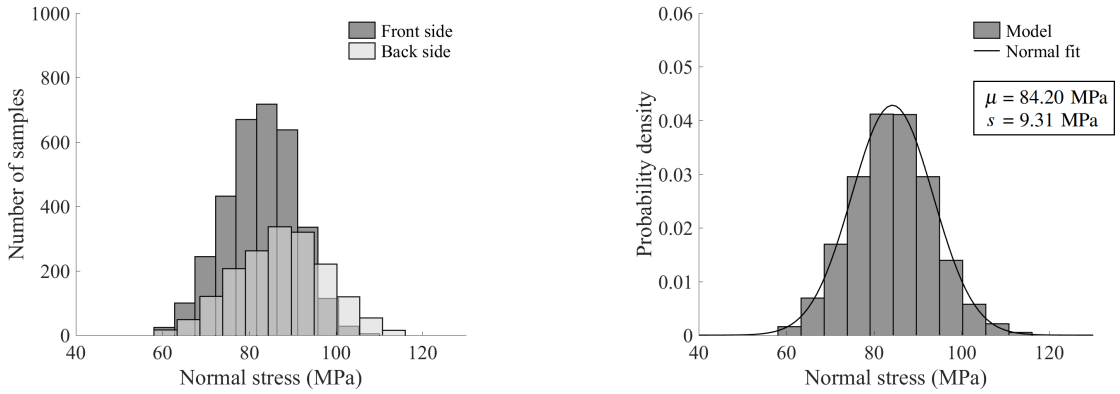

(a) (b)

Figure 29: The distribution of normal stresses at failure determined by the strength prediction model for the quasi-static pressure tests (a) divided in front and back failure, (b) including a fitted normal probability density function with corresponding parameters.

5. Discussion and concluding remarks

In this work, a further development of the strength prediction model proposed by Yankelevsky [12] has been presented. The model seeks to determine the fracture strength of glass without the need of experimental tests, and is based on the presence of microscopic surface flaws. These flaws are known to govern the fracture strength of glass, and lead to a highly probabilistic behaviour.

In an attempt to validate the strength prediction model, three different types of experiments on annealed float glass were conducted. These included quasi-static four-point bending tests on specimens of various size, and quasi-static and dynamic pressure tests on larger plates. As expected, the fracture strength varied within the same test setup, and was dependent on both the size of the glass plate and the loading condition.

The strength prediction model was able to successfully capture the trends observed in the quasi-static four-point bending tests. In the experiments, the mean strength seemed to increase with a decreasing specimen size; a trend the model also displayed. Additionally, the experimental fracture load was within the limits determined by the model. In the case of the quasi-static pressure tests, the fracture load obtained in the experiments was partly achieved by the strength prediction model. Specifically, the tests resulted in a slightly lower fracture strength than predicted by the model. This may be explained by an inaccurate value of the maximum flaw size. However, it may also be due to subcritical crack growth in the experiments, i.e., stable crack growth before failure. In fact, the quasi-static pressure tests lasted over twice as long as the longest-lasting bending tests. Consequently, this effect would be larger for the pressure tests.

Perhaps the largest source of error in the model arises in the modelling of the dynamic tests. The failure percentage determined by the model did not particularly coincide with the ones obtained in the experimental tests. It should, however, be noted that the number of experimental tests was limited. Nonetheless, the time and position of fracture initiation were captured by the strength prediction model. In order to consider dynamic effects, an incubation time, τ, was introduced. Since it was shown that the results were rather insensitive to the incubation time, a value of 10 µs was merely chosen. The strain rate effects on the glass' fracture strength may need to be included by different means, e.g. by including a fracture toughness dependent on strain rate. It was found that an increase in fracture toughness resulted in both increased fracture capacity and time to fracture.

The proposed model is simple, with few input parameters and cannot be expected to capture all effects arising in physical tests. It seems that the current model gives conservative solutions to the dynamic tests, whereas for the longer-lasting quasi-static tests, non-conservative solutions are obtained. Additionally, the chosen input parameters will need to be further investigated. This particularly applies to the flaw size and distribution. However, the model seems to have potential

as it manages to display many of the trends found in the experiments. The model can therefore contribute to a greater understanding and a more predictive modelling of the stochastic behaviour of glass plates under quasi-static and dynamic loading. In addition, the time it takes to perform the analyses of the strength prediction model is only a fraction of the time it takes to perform actual tests. This makes the model even more appealing to the user.

In a further work by the authors, the strength prediction model will be coupled with a finite element solver, so that numerical simulations of both failure and crack propagation in window glasses exposed to dynamic loading can be predicted.

6. Acknowledgements

The present work has been carried out with financial support from CASA (project number 237885), Centre for Research-based Innovation (CRI), at the Norwegian University of Science and Technology (NTNU). The authors would like to acknowledge Mr. Trond Auestad and Mr. Tore Wisth for assistance with the various experimental programmes. We would also like to thank the master students Mr. Kristoffer Aune Brekken, Mr. Petter Tønsberg Ingier, Ms. Nora Storebø Næss, Mr. Mathias Kolsaker and Mr. Ola Bratsberg for their contributions to this study. Acknowledgements are also expressed to Modum Glassindustri and Glassmester K. Larsen & Co for providing glass specimens for use in the experimental program.

References

[1] K. Spiller, J. A. Packer, M. V. Seica, D. Z. Yankelevsky, Prediction of annealed glass window response to blast loading, International Journal of Impact Engineering 88 (2016) 189–200.

[2] X. Zhang, H. Hao, Z. Wang, Experimental study of laminated glass window responses under impulsive and blast loading, International Journal of Impact Engineering 78 (2015) 1–19.

[3] M. Larcher, G. Solomos, F. Casadei, N. Gebbeken, Experimental and numerical investigations of laminated glass subjected to blast loading, International Journal of Impact Engineering 39 (1) (2012) 42–50.

[4] P. Hooper, R. Sukhram, B. Blackman, J. Dear, On the blast resistance of laminated glass, International Journal of Solids and Structures 49 (6) (2012) 899–918.

[5] J. Pelfrene, J. Kuntsche, S. Van Dam, W. Van Paepegem, J. Schneider, Critical assessment of the post-breakage performance of blast loaded laminated glazing: Experiments and simulations, International Journal of Impact Engineering 88 (2016) 61–71.

[6] H. D. Hidallana-Gamage, D. P. Thambiratnam, N. J. Perera, Failure analysis of laminated glass panels subjected to blast loads, Engineering Failure Analysis 36 (2014) 14–29.

[7] W. L. Beason, J. R. Morgan, Glass failure prediction model, Journal of Structural Engineering 110 (2) (1984) 197–212.

[8] J. B. Wachtman, W. R. Cannon, M. J. Matthewson, Mechanical properties of ceramics, 2nd Edition, John Wiley & Sons, 2009.

[9] W. Weibull, A statistical distribution function of wide applicability, Journal of Applied Mechanics 103 (730) (1951) 293–297.

[10] I. Nurhuda, N. Lam, E. Gad, I. Calderone, Estimation of strengths in large annealed glass panels, International Journal of Solids and Structures 47 (18) (2010) 2591–2599.

[11] C. Przybilla, A. Fernández-Canteli, E. Castillo, Deriving the primary cumulative distribution function of fracture stress for brittle materials from 3-and 4-point bending tests, Journal of the European Ceramic Society 31 (4) (2011) 451–460.

[12] D. Z. Yankelevsky, Strength prediction of annealed glass plates – A new model, Engineering Structures 79 (2014) 244–255.

[13] D. Z. Yankelevsky, K. Spiller, J. Packer, M. V. Seica, Fracture characteristics of laboratory-tested soda lime glass specimens, Canadian Journal of Civil Engineering 160 (2016) 151–160.

[14] V. Aune, E. Fagerholt, M. Langseth, T. Børvik, A shock tube facility to generate blast loading on structures, International Journal of Protective Structures 7 (3) (2016) 340–366.

[15] S. M. Wiederhorn, Fracture surface energy of glass, Journal of the American Ceramic Society 52 (2) (1969) 99–105.

[16] G. Anstis, P. Chantikul, B. R. Lawn, D. Marshall, A critical evaluation of indentation techniques for measuring fracture toughness: I, Direct crack measurements, Journal of the American Ceramic Society 64 (9) (1981) 533–538.

[17] NS-EN 572-1: Glass in building – Basic soda-lime silicate glass products – Part 1: Definitions and general physical and mechanical properties, Standard, CEN (2012).

[18] NS-EN 13541: Glass in building – Security glazing- Testing and classification of resistance against explosion pressure, Standard, CEN (2012).

[19] ASTM C1161-13, Standard Test Method for Flexural Strength of Advanced Ceramics at Ambient Temperature, Standard, ASTM International, West Conshohocken, PA (2013).

[20] M. Lindqvist, C. Louter, Experimental study on glass edge machining flaw characterization, Engineering Fracture Mechanics 127 (2014) 56–70.

[21] D. Cormie, G. Mays, P. Smith, Blast effects on buildings, 2nd Edition, Thomas Telford Publishing, 2009.

[22] V. Aune, G. Valsamos, F. Casadei, M. Larcher, M. Langseth, T. Børvik, Numerical study on the structural response of blast-loaded thin aluminium and steel plates, International Journal of Impact Engineering 99 (2017) 131–144.

[23] E. Fagerholt, Field measurements in mechanical testing using close-range photogrammetry and digital image analysis, Ph.D. thesis, Norwegian University of Science and Technology (NTNU), Trondheim (2012).

[24] M. Yoda, Subcritical crack growth of glass, Engineering Fracture Mechanics 28 (1) (1987) 77–84.

[25] T. L. Anderson, Fracture mechanics: Fundamentals and Applications, 3rd Edition, CRC press, 2005.

[26] G. R. Irwin, Analysis of stresses and strains near the end of a crack traversing a plate, Journal of Applied Mechanics 24 (3) (1957) 361–364.

[27] J. Newman, I. Raju, An empirical stress-intensity factor equation for the surface crack, Engineering Fracture Mechanics 15 (1-2) (1981) 185–192.

[28] W. Levengood, Effect of origin flaw characteristics on glass strength, Journal of Applied Physics 29 (5) (1958) 820–826.

[29] A. A. Wereszczak, M. K. Ferber, W. Musselwhite, Method for identifying and mapping flaw size distributions on glass surfaces for predicting mechanical response, International Journal of Applied Glass Science 5 (1) (2014) 16–21.

[30] NS-EN 572-1: Glass in building – Basic soda-lime silicate glass products – Part 2: Float glass, Standard, CEN (2012).

[31] Abaqus, Version 6.14, Dassault Systèmes Simulia Corporation, Providence, RI, USA, 2014.

[32] Y. V. Petrov, N. Morozov, V. Smirnov, Structural macromechanics approach in dynamics of fracture, Fatigue & Fracture of Engineering Materials & Structures 26 (4) (2003) 363–372.

[33] X. Zhang, Y. Zou, H. Hao, X. Li, G. Ma, K. Liu, Laboratory test on dynamic material properties of annealed float glass, International Journal of Protective Structures 3 (4) (2012) 407–430.

[34] M. Peroni, G. Solomos, V. Pizzinato, M. Larcher, Experimental investigation of high strain-rate behaviour of glass, Applied Mechanics and Materials 82 (2011) 63–68.